



### Controlling 3-D Morphology of Ni-Fe-Based Nanocatalysts for Oxygen Evolution Reaction

Journal:	<i>Nanoscale</i>
Manuscript ID	NR-ART-12-2018-010138.R1
Article Type:	Paper
Date Submitted by the Author:	26-Jan-2019
Complete List of Authors:	<p>Manso, Ryan; University of Arkansas, Chemistry and Biochemistry  Acharya, Prashant; University of Arkansas, Chemical Engineering  Deng, Shiqing; Brookhaven National Laboratory, Condensed Matter Physics and Materials Science Department; Tsinghua University, School of Materials Science and Engineering  Crane, Cameron; University of Arkansas, Chemistry and Biochemistry  Reinhart, Benjamin; Argonne National Laboratory, X-Ray Sciences Division  Lee, Sungsik; APS,  Tong, Xiao; Brookhaven National Laboratory, Center for functional Nanomaterials  Nykypanchuk, Dmytro; Brookhaven National Laboratory , Center for Functional Nanomaterials  Zhu, Jing; Tsinghua University, School of Materials Science and Engineering  Zhu, Yimei; Brookhaven National Laboratory,  Greenlee, Lauren; University of Arkansas, Ralph E. Martin Department of Chemical Engineering  Chen, Jingyi; University of Arkansas, Chemistry and Biochemistry</p>

1

2 **Controlling 3-D Morphology of Ni-Fe-Based Nanocatalysts for Oxygen Evolution Reaction**

3

4 Ryan H. Manso,<sup>1,†</sup> Prashant Acharya,<sup>2,†</sup> Shiqing Deng,<sup>3,4†</sup> Cameron C. Crane,<sup>1</sup> Benjamin  
5 Reinhart,<sup>5</sup> Sungsik Lee,<sup>5</sup> Xiao Tong,<sup>6</sup> Dmytro Nykypanchuk,<sup>6</sup> Jing Zhu,<sup>4</sup> Yimei Zhu,<sup>3</sup> Lauren F.  
6 Greenlee,<sup>2,\*</sup> and Jingyi Chen<sup>1,\*</sup>

7

8 <sup>1</sup>Department of Chemistry and Biochemistry, University of Arkansas, Fayetteville, AR 72701,  
9 USA

10 <sup>2</sup>Ralph E. Martin Department of Chemical Engineering, University of Arkansas, Fayetteville, AR  
11 72701, USA

12 <sup>3</sup>Condensed Matter Physics and Materials Science Department, Brookhaven National Laboratory,  
13 Upton, NY 11973, USA

14 <sup>4</sup>School of Materials Science and Engineering, Tsinghua University, Beijing 100084, P. R. China

15 <sup>5</sup>Advanced Photon Source, Argonne National Laboratory, Lemont, IL 60439, USA

16 <sup>6</sup>Center for Functional Nanomaterials, Brookhaven National Laboratory, Upton, NY 11973, USA

17

18 <sup>†</sup>These authors contributed to this work equally.

19 <sup>\*</sup>Corresponding authors: chenj@uark.edu (synthesis, characterization) and greenlee@uark.edu  
20 (electrocatalysis, characterization)

21

22 **Abstract:** Controlling the 3-D morphology of nanocatalysts is one of the underexplored but  
23 important approaches for improving the sluggish kinetics of oxygen evolution reaction (OER) in  
24 water electrolysis. This work reports a scalable, oil-based method based on thermal  
25 decomposition of organometallic complexes to yield highly uniform Ni-Fe-based nanocatalysts  
26 with well-defined morphology (i.e., Ni-Fe core-shell, Ni/Fe alloy, and Fe-Ni core-shell).  
27 Transmission electron microscopy reveals their morphology and composition to be NiO<sub>x</sub>-  
28 FeO<sub>x</sub>/NiO<sub>x</sub> core-mixed shell, NiO<sub>x</sub>/FeO<sub>x</sub> alloy, and FeO<sub>x</sub>-NiO<sub>x</sub> core-shell. X-ray techniques  
29 resolve the electronic structures of the bulk and are supported by electron energy loss  
30 spectroscopy analysis of individual nanoparticles. These results suggest the crystal structure of  
31 Ni is most likely to contain  $\alpha$ -Ni(OH)<sub>2</sub> and that the chemical environment of Fe is variable,  
32 depending on the morphology of the nanoparticle. The Ni diffusion from the amorphous Ni-  
33 based core to the iron oxide shell makes the NiO<sub>x</sub>-NiO<sub>x</sub>/FeO<sub>x</sub> core-mixed shell structure the most  
34 active and the most stable nanocatalyst, which outperforms the comparison NiO<sub>x</sub>/FeO<sub>x</sub> alloy  
35 nanoparticles expected to be active for OER. This study suggests that the chemical environment  
36 of the mixed NiO<sub>x</sub>/FeO<sub>x</sub> alloy composition is important to achieve high electrocatalytic activity  
37 for OER and that the 3-D morphology plays a key role in optimization of the electrocatalytic  
38 activity and stability of the nanocatalyst for OER.

39

40

41

## 42 **Introduction**

43 Water electrolysis can be employed to produce hydrogen and oxygen as an alternative, more  
44 environmentally friendly means to generate clean renewable fuels.<sup>1-2</sup> In principle, water splitting  
45 is straightforward, separating into two half reactions on the cathode (hydrogen evolution reaction,  
46 HER) and anode (oxygen evolution reaction, OER), but the efficiency of the overall reaction  
47 remains limited. One of the major obstacles is the slow kinetics of the four-electron OER, which  
48 requires a much greater applied potential than the thermodynamic standard potential.<sup>1</sup> Finding  
49 catalytic materials to lower the amount of potential applied above the thermodynamic  
50 requirement (i.e., overpotential) remains a necessary task to allow potential viable  
51 commercialization of water electrolysis. Electrocatalysts based on noble metals such as Pt, Ru, Ir,  
52 and their oxides have been extensively investigated for OER due to appreciable activity and  
53 relatively high stability.<sup>3-4</sup> Compared to Pt, Ru, and Ir, their oxides were better catalysts with  
54 relatively low overpotentials, and thus RuO<sub>x</sub> and IrO<sub>x</sub> have been recommended as benchmarks in  
55 the development of active electrocatalysts for OER.<sup>5-7</sup> Despite their superior performance, the  
56 high cost of these scarce materials makes their choice difficult for large-scale industrial use. It is  
57 a critical need to search for inexpensive materials with high catalytic performance for OER to  
58 enable practical use in water electrolyzers.

59 The earth-abundant 3-*d* transition metal-based materials such as Mn, Fe, Co, and Ni oxides  
60 and hydroxides have emerged as promising catalyst candidates for OER under alkaline  
61 conditions.<sup>8-12</sup> Among these low-cost oxides and hydroxides, the Ni-Fe-based materials are  
62 among the most active catalysts, with catalytic activity for OER comparable to that of RuO<sub>x</sub> and  
63 IrO<sub>x</sub>.<sup>13-15</sup> Early studies on Ni-based alkaline batteries found that the presence of Fe could lower  
64 the OER overpotential on Ni-based electrodes.<sup>16-17</sup> In the 1980s, Corrigan first reported that the

65 synergistic effects of Fe and Ni on OER activity were the result of a Ni-Fe hydrous oxide  
66 composite with markedly different electrochemical properties compared to either monometallic  
67 material alone.<sup>18</sup> Since then, mixed Ni-Fe-based thin films have been extensively investigated  
68 through electrochemical methods,<sup>19-25</sup> *in situ* spectroscopic tools (e.g., Mössbauer  
69 spectroscopy,<sup>26-28</sup> Raman spectroscopy,<sup>29-31</sup> and x-ray absorption spectroscopy<sup>32-39</sup>) and density  
70 functional theory<sup>36, 40-42</sup> in an effort to understand reaction mechanisms and elucidate structure-  
71 activity relationships. The early study by Corrigan indicated that coprecipitating as little as 0.01%  
72 Fe could significantly lower the overpotential for OER.<sup>18</sup> Later, it was confirmed by other groups  
73 that Fe impurities in the electrolyte could substantially improve the OER activity of Ni-only  
74 materials.<sup>19, 36</sup> The optimal activity varied with the Fe composition in the films, with some  
75 studies showing similar performance in the range between 10-50%<sup>18, 29</sup> and others indicating 25%  
76 to be the optimum.<sup>19-20</sup> The discrepancy in optimal composition for improved OER activity may  
77 be due to the difference in the preparation methods and the resulting structures of these mixed  
78 Ni-Fe-based thin films. The commonly-used electrodeposition usually generates layered  
79 hydroxide structures, while other synthesis methods can produce different Ni-Fe-based structures.  
80 For example, thermal annealing generated a Fe<sub>3</sub>O<sub>4</sub>-based spinel structure hosted with Ni  
81 substitution, forming NiFe<sub>2</sub>O<sub>4</sub>,<sup>34</sup> while an aerosol-spray-assisted approach produced Ni-Fe-based  
82 amorphous materials.<sup>43</sup>

83 Since Ni-Fe-based materials appear to be one of the most active catalysts for OER in these  
84 thin film studies, progress has been recently made to reduce the dimension of these active Ni-Fe-  
85 based materials for improved OER activity. For example, single-layer nanosheets generated by  
86 liquid phase exfoliation of the layered double hydroxides exhibited significantly higher OER  
87 activity than their bulk counterparts.<sup>44</sup> More recent studies by *in situ* electrochemical atomic

88 force microscopy illustrated the structural dynamics of these nanosheets under electrochemical  
89 conditions.<sup>45-46</sup> On the other hand, nanoscale spinel-type Ni-Fe based oxides were synthesized by  
90 a solvothermal method and showed that the  $\text{Ni}_x\text{Fe}_{3-x}\text{O}_4/\text{Ni}$  nanocomposite with an  $x$  value of  
91  $\sim 0.36$  exhibited the most superior activity for OER.<sup>47</sup> While nanocatalysts show promise to  
92 improve OER activity, little effort has been made to explore the morphological effects on the  
93 electrocatalytic performance of Ni-Fe-based nanocatalysts. Our previous multistep aqueous-  
94 based synthesis of Ni-Fe-based nanocatalysts demonstrated that a core-shell morphology having  
95 a  $\text{Fe}/\text{Fe}(\text{OH})_3$  core and a  $\text{Fe}_x\text{Ni}_{1-x}(\text{OH})_2$  shell exhibited a superior OER activity.<sup>48</sup> In this work,  
96 we developed a scalable, oil-based synthesis approach based on thermal decomposition of  
97 organometallic complexes that enables manipulation of both the morphology and crystalline  
98 phase of the Ni-Fe nanocatalysts. Highly uniform Ni-Fe-based nanostructures with different  
99 morphologies (i.e., core-shell and alloy) were synthesized *via* either sequential or simultaneous  
100 injection. The uniform nanostructures enabled us to use transmission electron microscopy (TEM)  
101 for in-depth structural and electronic characterization of a single particle. Together with the x-ray  
102 methods on the bulk sample, we elucidate the morphology, composition, and structure of  
103 individual particles for each of these nanostructures in detail. We then evaluate the OER  
104 performance for these well-defined, Ni-Fe-based nanostructures with Ni and Fe alone  
105 nanoparticles. This study allows us to establish a fundamental understanding of as-synthesized  
106 morphological, compositional, and structural influences on the electrocatalytic activity of Ni-Fe-  
107 based nanocatalysts for OER.

## 108 **Results and Discussion**

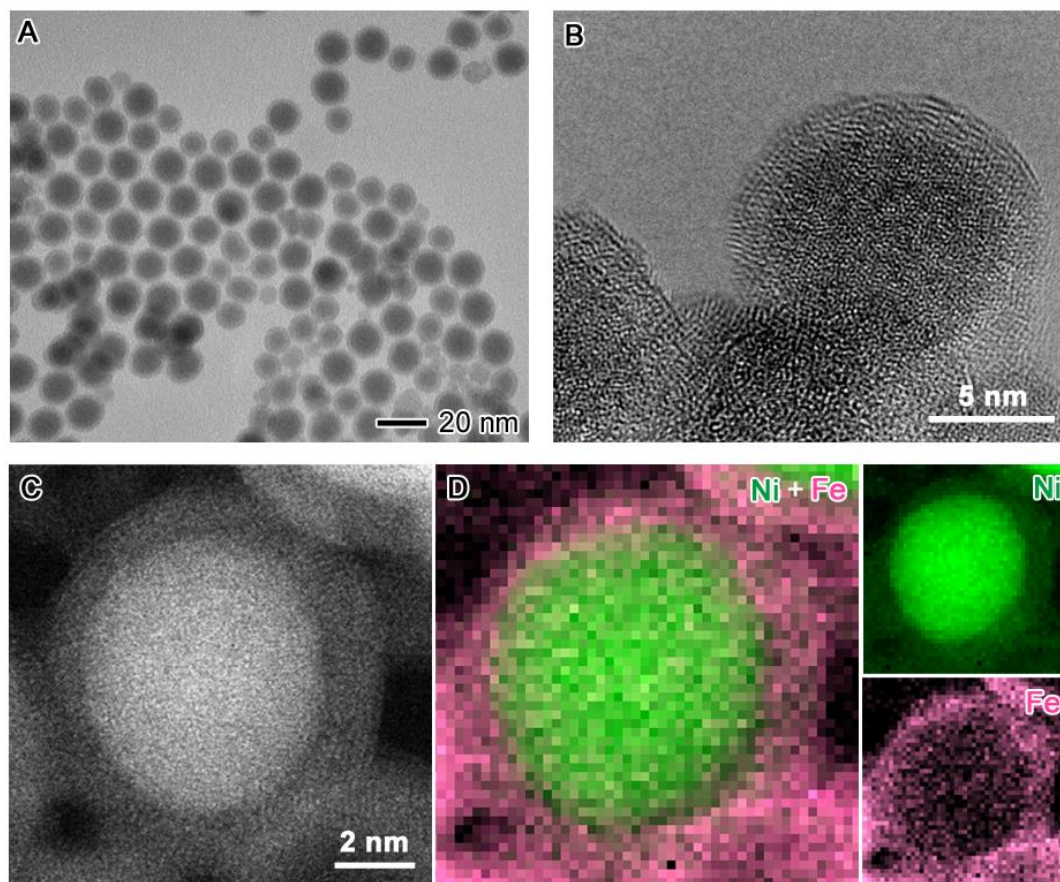
109 Three Ni-Fe-based nanostructures with different morphologies were designed and  
110 synthesized for this study and included Ni-Fe-based core-shell, Ni-Fe-based alloy, and Fe-Ni-

111 based core-shell. Nanostructure synthesis was achieved through solution-based thermal  
112 decomposition of organometallic complexes in high-boiling-temperature organic solvent.  
113 Programmable temperature control was used to improve the uniformity of the resulting  
114 nanoparticles. The core-shell structures were synthesized using a two-step procedure with the  
115 first step to synthesize the cores, followed by the second step to coat the cores with the shells.  
116 The alloy structures were prepared in a one-step synthesis by simultaneously injecting both  
117 precursors into the solvent. During synthesis, the nanoparticles are oxidized when exposed to the  
118 ambient atmosphere, and thus we denote the resulting Ni-Fe-based nanostructures as nickel  
119 oxides ( $\text{NiO}_x$ ) and iron oxides ( $\text{FeO}_x$ ). After synthesis, the nanoparticles were transferred from  
120 the organic phase into aqueous solution through ligand exchange process using polyethylene  
121 glycol terminated with carboxylic acid (PEG-COOH). The overall reaction yield is ~70% and the  
122 estimated cost for the synthesis was listed in **Table S1**. The analytical TEM, XPS, XRD, and  
123 XAS, as well as the electrochemical characterization were performed on the nanoparticles with  
124 PEG-COOH as surface ligands.

125  $\text{NiO}_x$ - $\text{FeO}_x$  core-shell nanoparticles were synthesized by thermally decomposing  $\text{Fe}(\text{CO})_5$   
126 complex in the presence of preformed  $\text{NiO}_x$  seeds. **Figure 1A** displays a representative TEM  
127 image of the reaction product, indicating a core-shell morphology of the nanoparticles. These  
128 nanoparticles are relatively uniform with an overall diameter of  $16.8 \pm 2.0$  nm. The size of the  
129 core  $\text{NiO}_x$  nanoparticles is  $12.4 \pm 0.6$  nm (**Figure S1**), and the shell thickness of the core-shell  
130 nanoparticles is estimated to be ~2.2 nm. The x-ray photoelectron spectroscopy (XPS) study  
131 indicates that the binding energies of Fe  $2p_{3/2}$  and Ni  $2p_{3/2}$  of the core-shell nanoparticles are at  
132 711.5 eV and ~856.4 eV, respectively, confirming the formation of  $\text{FeO}_x$  and  $\text{NiO}_x$  (**Figure S2**).

133 Further characterization of an individual nanoparticle using high-resolution transmission  
134 electron microscopy (HRTEM) and high-angle annular dark-field-scanning transmission electron  
135 microscopy (HAADF-STEM) imaging clearly showed a core-shell morphology, but rather poor  
136 crystallinity (**Figure 1, B and C**). The corresponding electron energy-loss spectroscopy (EELS)  
137 mapping of the individual nanoparticle in the HAADF-STEM image reveals elemental  
138 distribution of a Ni-Fe core-shell structure (**Figure 1D**). Quantitative analysis of the EELS  
139 mapping reveals that the overall atomic ratio of Ni to Fe for individual  $\text{NiO}_x$ - $\text{NiO}_x/\text{FeO}_x$  core-  
140 mixed shell nanoparticles is around 1.36 to 1, close to the 1:1 ratio obtained through inductively  
141 coupled plasma mass spectrometry (ICP-MS) of the sample. It is worth noting that Ni is not  
142 confined in the core but diffuses into the shell. The composition of the shell was analyzed by  
143 extracting the signals of Ni and Fe in the ring region, where the shell is projected in the 2-D  
144 EELS map (**Figure S3**). The quantitative analysis indicates that a 0.39:1 atomic ratio of Ni:Fe is  
145 present in the shell corresponding to atomic percent of 28% Ni and 72% Fe. Therefore, the  $\text{NiO}_x$ -  
146  $\text{FeO}_x$  core-shell nanoparticles are actually made of a  $\text{NiO}_x$  core and a  $\text{NiO}_x/\text{FeO}_x$  mixed shell,  
147 denoted as  $\text{NiO}_x$ - $\text{NiO}_x/\text{FeO}_x$  core-mixed shell structures.



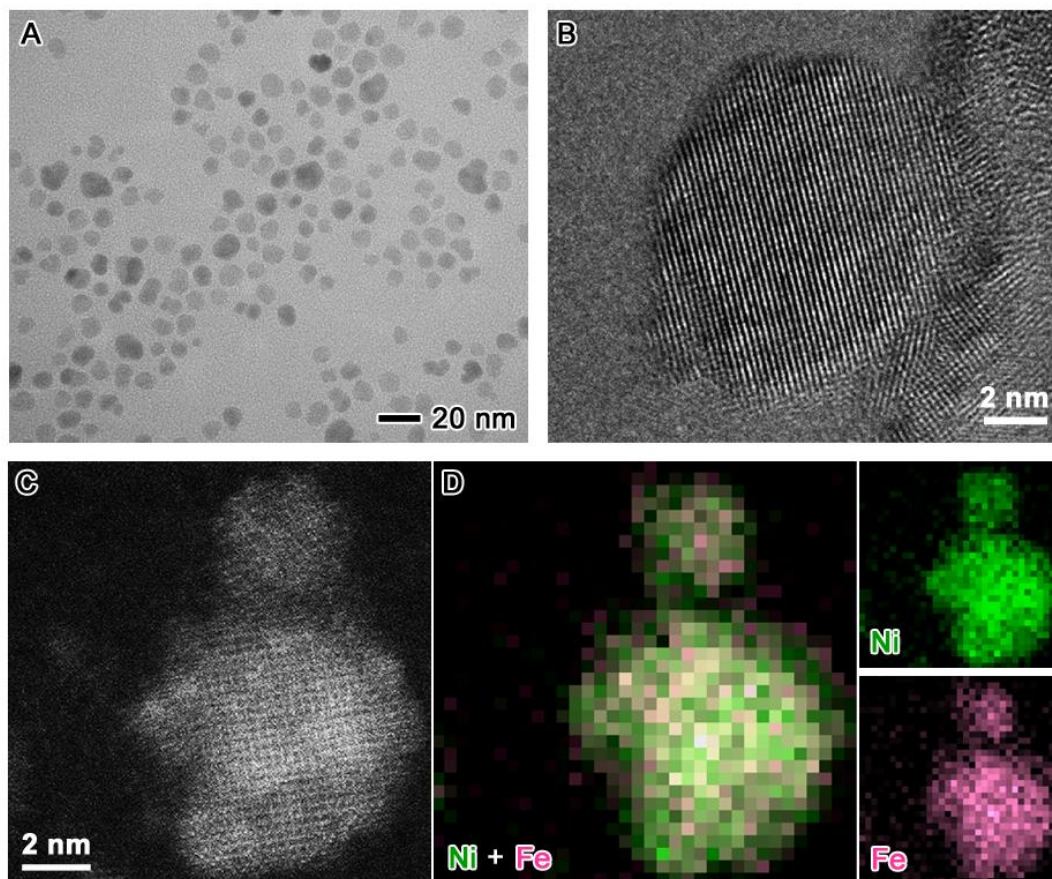


148  
149  
150 **Figure 1.** Electron microscopy characterization of NiO<sub>x</sub>-NiO<sub>x</sub>/FeO<sub>x</sub> core-mixed shell  
151 nanoparticles: (A) TEM image overview of the nanoparticles with an average diameter of 16.8 ±  
152 2.0 nm; (B,C) HRTEM and HAADF-STEM images displaying a representative nanoparticle in  
153 (A) which is mostly amorphous; (D) EELS mapping of the nanoparticle in (C) with Ni (green),  
154 Fe (pink), and Ni-Fe overlaid maps indicating a NiO<sub>x</sub>-NiO<sub>x</sub>/FeO<sub>x</sub> core-mixed shell morphology.  
155 The Ni/Fe atomic ratio of the shell is 0.39:1.  
156

157 NiO<sub>x</sub>/FeO<sub>x</sub> alloy nanoparticles were prepared using a similar procedure to that of NiO<sub>x</sub>  
158 preparation except that the reactant Ni(acac)<sub>2</sub> alone in the NiO<sub>x</sub> synthesis was replaced by the  
159 mixture of Ni(acac)<sub>2</sub> and Fe(acac)<sub>3</sub> at a 1:1 molar ratio in the alloy nanoparticle synthesis. From  
160 the TEM image in **Figure 2A**, the alloy nanoparticles appear to be more or less spherical in  
161 shape but are less uniform and slightly smaller compared to NiO<sub>x</sub> nanoparticles. The average size  
162 of the alloy nanoparticles is 9.4 ± 1.7 nm. HRTEM image clearly shows the lattice fringes of an  
163 alloy nanoparticle, indicating good crystallinity (**Figure 2B**). No obvious contrast difference is

164 observed in the HAADF-STEM image, suggesting homogenous distributions of Ni and Fe in a  
165 single, or similar density, phase(s) across the entire nanoparticle (**Figure 2C**). The corresponding  
166 EELS mapping agrees with the observations made from HAADF-STEM image contrast, wherein  
167 Ni and Fe are co-localized evenly across the nanoparticle, indicating an alloy composition  
168 (**Figure 2D**). The XPS spectra of the NiO<sub>x</sub>/FeO<sub>x</sub> nanoparticles in **Figure S2** indicate that the  
169 peak position of the Fe 2p<sub>3/2</sub> and Ni 2p<sub>3/2</sub> binding energies are 712.1 eV and 857.1 eV,  
170 respectively, confirming the oxide formation. The NiO<sub>x</sub>/FeO<sub>x</sub> mixed oxides have higher binding  
171 energies than FeO<sub>x</sub> (710.7 eV for Fe 2p<sub>3/2</sub>) or NiO<sub>x</sub> (856.6 eV for Ni 2p<sub>3/2</sub>). Quantitative analysis  
172 of the EELS spectra indicates that the Ni/Fe atomic ratio of individual particles is ~0.8, which is  
173 close to ICP-MS analysis, showing the overall Ni/Fe atomic ratio of the sample to be 1:1.

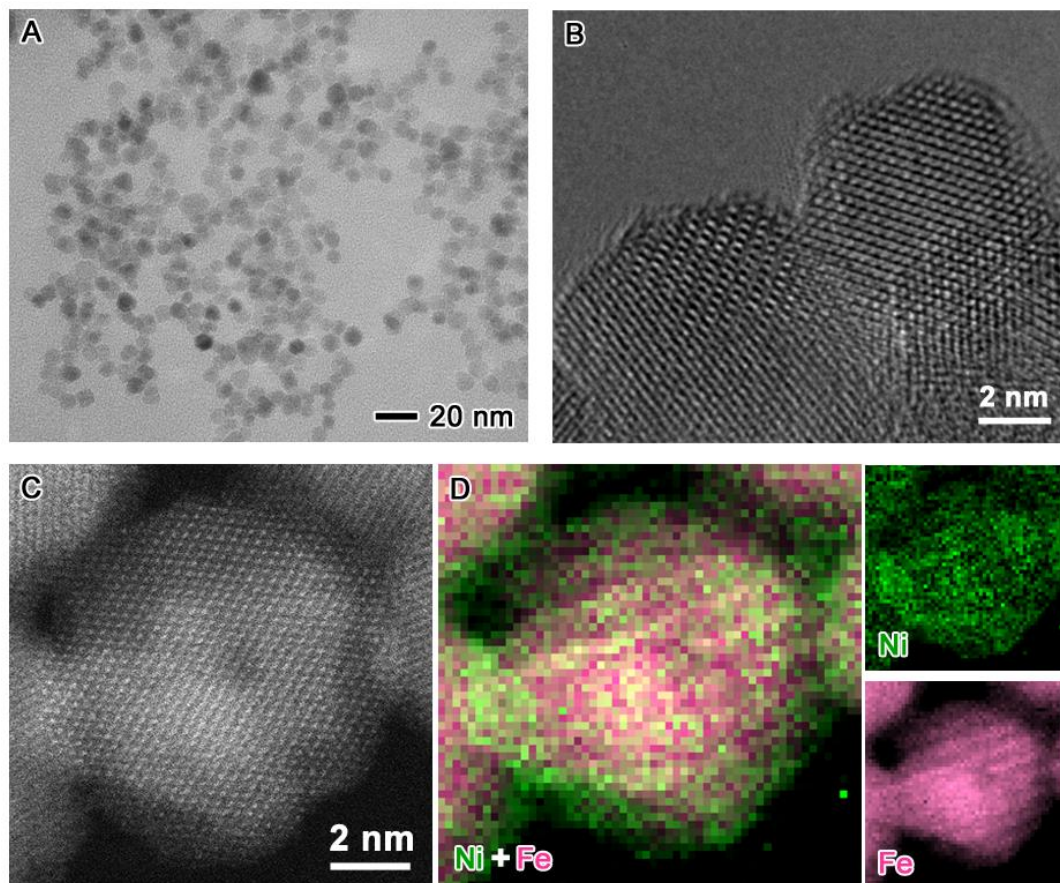
174



175

176  
177 **Figure 2.** Electron microscopy characterization of NiO<sub>x</sub>/FeO<sub>x</sub> alloy nanoparticles: (A) TEM  
178 image overview of the nanoparticles with an average diameter of  $9.4 \pm 1.7$  nm. (B,C) HRTEM  
179 and HAADF-STEM images displaying a representative nanoparticle in (A) which is crystalline;  
180 (D) EELS mapping of the nanoparticle in (C) with Ni (green), Fe (pink), and Ni-Fe overlaid  
181 maps indicating a NiO<sub>x</sub>/FeO<sub>x</sub> alloy composition.  
182

183 FeO<sub>x</sub>-NiO<sub>x</sub> core-shell nanoparticles were also synthesized using a two-step procedure by first  
184 generating the FeO<sub>x</sub> nanoparticles and then coating them with NiO<sub>x</sub> shells. The FeO<sub>x</sub>  
185 nanoparticles were prepared by thermally decomposing Fe(acac)<sub>3</sub> in a mixture of dibenzyl ether  
186 and oleylamine. These FeO<sub>x</sub> nanoparticles are spherical in shape with an average diameter of  $9.0$   
187  $\pm 1.7$  nm according to TEM imaging (**Figure S4**). The coating process was performed using  
188 thermal decomposition of bis(1,5-cyclooctadienenickel(0)) (Ni(COD)<sub>2</sub>) in the presence of the  
189 FeO<sub>x</sub> nanoparticles. After coating with the Ni shells, the FeO<sub>x</sub>-NiO<sub>x</sub> core-shell nanoparticles  
190 have an average diameter of  $9.8 \pm 1.6$  nm, as shown in **Figure 3A**. The shell thickness is  
191 estimated to be  $\sim 0.4$  nm. HRTEM result suggests that the nanoparticles exhibit a good  
192 crystallinity of the FeO<sub>x</sub> core, which is covered with an amorphous NiO<sub>x</sub> shell (**Figure 3B**). In  
193 the HAADF-STEM image, the contrast does not show an obvious core-shell structure (**Figure**  
194 **3C**); however, the EELS mapping of an individual nanoparticle indicates that the Ni signal  
195 covers a slightly larger area, as compared to the Fe signal (**Figure 3D**). The Ni/Fe ratio of the  
196 entire nanoparticle was calculated to be around 0.078:1, corresponding to atomic percent 7.2%  
197 Ni, which is much less than that measured from ICP-MS (18.0% Ni). This difference could be  
198 attributed to the presence of pure Ni, possibly from leached Ni or from homogenous, nucleated  
199 Ni. The XPS spectra of the FeO<sub>x</sub>-NiO<sub>x</sub> core-shell nanoparticles in **Figure S3** confirm the oxide  
200 composition with the peak positions of the Fe 2p<sub>3/2</sub> and Ni 2p<sub>3/2</sub> binding energies to be 710.7 eV  
201 and 855.5 eV, respectively.



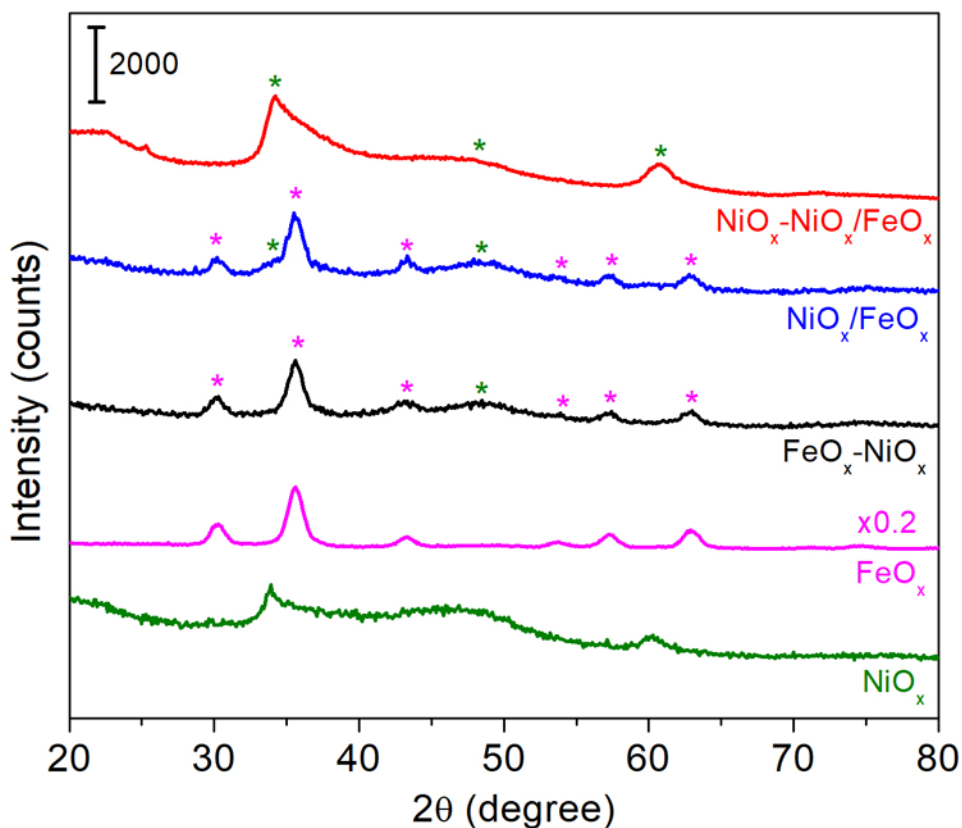
202

203 **Figure 3.** Electron microscopy characterization of  $\text{FeO}_x\text{-NiO}_x$  core-shell nanoparticles: (A) TEM  
 204 image overview of the nanoparticles with an average diameter of  $9.8 \pm 1.6$  nm; (B,C) HRTEM  
 205 and HAADF-STEM images displaying a representative nanoparticle in (A) with a crystalline  
 206 core and a thin amorphous shell; (D) EELS mapping of the nanoparticle in (C) with Ni (green),  
 207 Fe (pink), and Ni-Fe overlaid maps, confirming the core-shell structure.

208

209 The crystal structures of these Ni-Fe-based nanoparticles were analyzed by x-ray powder  
 210 diffraction (XRD) on the bulk samples, as shown in **Figure 4**. The XRD pattern of the  $\text{NiO}_x$   
 211 nanoparticles indicates three broad peaks at  $30.4^\circ$ ,  $47.0^\circ$ , and  $60.1^\circ$ , which can be indexed to  $\alpha$ -  
 212  $\text{Ni}(\text{OH})_2$  with Ni(II) valence.<sup>49-50</sup> The weak and broad XRD signals are ascribed to the lack of  
 213 long-range order in the  $\alpha$ - $\text{Ni}(\text{OH})_2$  crystal structure. According to the XRD pattern, the  $\text{FeO}_x$   
 214 nanoparticles could be composed of  $\gamma\text{-Fe}_2\text{O}_3$  with Fe(III) valance and/or  $\text{Fe}_3\text{O}_4$  with mixed  
 215 valence of Fe(II) and Fe(III). Since  $\text{Fe}(\text{acac})_3$  with  $\text{Fe}^{3+}$  was used as the precursor, the  $\text{FeO}_x$

216 nanoparticles are likely to be  $\gamma$ -Fe<sub>2</sub>O<sub>3</sub>; however, we cannot rule out the possibility of the  
217 presence of Fe(II) in the form of Fe<sub>3</sub>O<sub>4</sub> because the reaction was carried out under a reducing  
218 environment with the presence of oleylamine.<sup>51</sup> The XRD pattern of the NiO<sub>x</sub>-NiO<sub>x</sub>/FeO<sub>x</sub> core-  
219 mixed shell nanoparticles is essentially the same as that of NiO<sub>x</sub> with three broad peaks at 30.4°,  
220 47.0°, and 60.1°, suggesting that the mixed NiO<sub>x</sub>/FeO<sub>x</sub> shell is largely amorphous consistent with  
221 HRTEM result in Figure 1B. According to our previous study, the thermal decomposition of  
222 Fe(CO)<sub>5</sub> at the early stage when reaction temperature was relatively low (180 °C) yielded mostly  
223 amorphous FeO<sub>x</sub>; if any crystallinity is present, it should be below the detection limit of XRD (<  
224 2%).<sup>52</sup> Based on these results, it is suggested that the core-shell nanoparticles are made of  $\alpha$ -  
225 Ni(OH)<sub>2</sub> and Fe<sub>3</sub>O<sub>4</sub>. For the NiO<sub>x</sub>/FeO<sub>x</sub> alloy nanoparticles, the XRD pattern appears to be a  
226 mixture of  $\alpha$ -Ni(OH)<sub>2</sub> and iron oxide(s). Similar to the FeO<sub>x</sub> nanoparticles, the FeO<sub>x</sub> in the alloy  
227 is likely to be  $\gamma$ -Fe<sub>2</sub>O<sub>3</sub> due to the same precursor Fe(acac)<sub>3</sub> used in the synthesis. Compared to  
228 that of the FeO<sub>x</sub> nanoparticles, the XRD pattern of FeO<sub>x</sub>-NiO<sub>x</sub> core-shell nanoparticles exhibits  
229 an additional broad peak at 47.0° that can be assigned to  $\alpha$ -Ni(OH)<sub>2</sub>. The weak  $\alpha$ -Ni(OH)<sub>2</sub> is due  
230 to a small amount (~10 atomic%) of Ni in the FeO<sub>x</sub>-NiO<sub>x</sub> core-shell nanoparticles. The presence  
231 of  $\alpha$ -Ni(OH)<sub>2</sub> as the primary phase for Ni atoms is promising for the OER because this more  
232 disordered phase of nickel hydroxide is now known to be the more active phase for alkaline  
233 OER.<sup>19</sup> The presence of peaks for iron oxide phases does suggest that at least some, or perhaps  
234 all, of the Fe atoms are present in a separate oxide phase in the as-synthesized nanoparticles.  
235 However, it is also possible that some of the Fe and Ni atoms are present in a combined  
236 hydroxide phase, as has been suggested for other Fe-Ni hydroxide/oxide materials.<sup>22, 36</sup>



237  
238

239 **Figure 4.** XRD patterns of different nanoparticle samples:  $\text{NiO}_x\text{-NiO}_x/\text{FeO}_x$  core-mixed shell  
240 (red),  $\text{NiO}_x/\text{FeO}_x$  alloy (blue),  $\text{FeO}_x\text{-NiO}_x$  core-shell (black),  $\text{FeO}_x$  (pink), and  $\text{NiO}_x$  (green). The  
241 peaks assigned to  $\alpha\text{-Ni(OH)}_2$  are labelled by green stars while the peaks indexed to  $\text{Fe}_3\text{O}_4$  or  $\gamma\text{-}$   
242  $\text{Fe}_2\text{O}_3$  are labelled by pink stars.

243

244 *Ex situ* XAS was performed on this series of nanocatalysts to examine the collective

245 composition and structure of each nanocatalyst. The spectra for Fe are plotted in **Figure 5**,

246 supplemented with a full set of Fe standard spectra plotted in **Figure S5**. The spectral shapes of

247 the Fe K-edge for  $\text{FeO}_x$  nanoparticles,  $\text{FeO}_x\text{-NiO}_x$  core-shell nanoparticles, and the  $\text{NiO}_x/\text{FeO}_x$

248 alloy nanoparticles appear quite similar. However, at the white line, the peak intensity is

249 noticeably different for the three samples, and the peak position of the edge is shifted slightly to

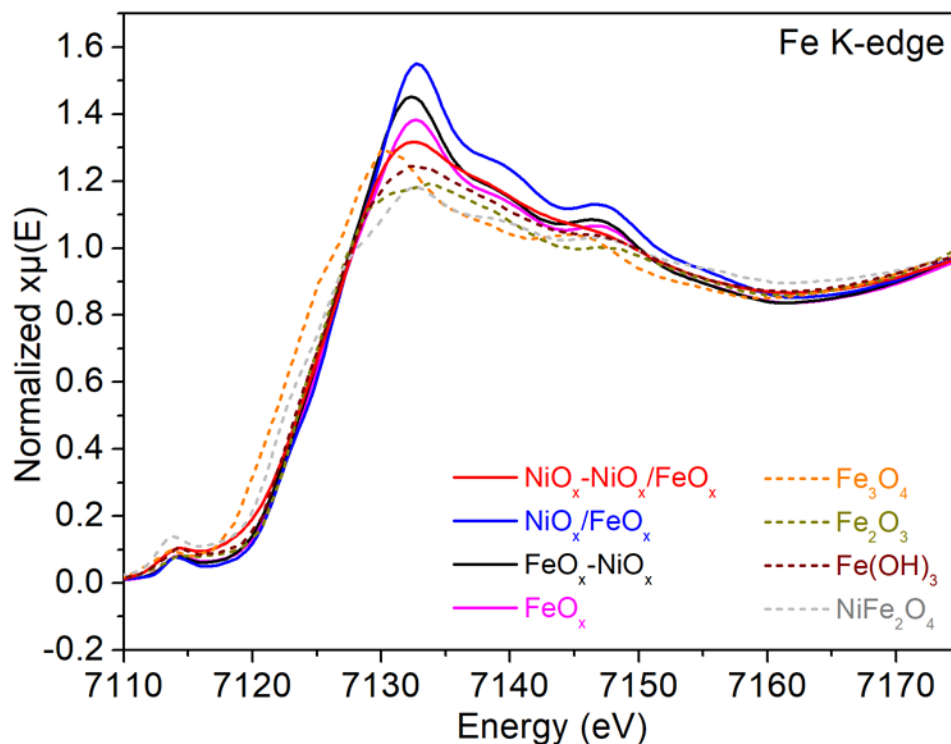
250 higher eV for  $\text{FeO}_x$  and  $\text{NiO}_x/\text{FeO}_x$ . When comparing across different sample morphologies and

251 metal compositions, an increase in peak height can suggest an increase in order or crystallinity,

252 while a shift to higher eV most likely suggests a larger portion of the Fe atoms are in a higher

253 oxidation state. These results support HRTEM and XRD results, where NiO<sub>x</sub>/FeO<sub>x</sub> and FeO<sub>x</sub>-  
254 NiO<sub>x</sub> nanoparticles were both found to be more crystalline than the NiO<sub>x</sub>-NiO<sub>x</sub>/FeO<sub>x</sub> core-mixed  
255 shell nanoparticle sample. The shift to slightly higher eV for FeO<sub>x</sub> suggests that more of the Fe  
256 atoms are likely to be in the 3+ oxidation state, rather than in the 2+ oxidation state, a conclusion  
257 that is also supported by the discussion above and the use of a Fe<sup>3+</sup> precursor during synthesis.  
258 Similarly, the NiO<sub>x</sub>/FeO<sub>x</sub> alloy nanoparticle sample, also synthesized from the Fe<sup>3+</sup> precursor,  
259 has an edge position that is shifted slightly to higher eV, as compared to the FeO<sub>x</sub>-NiO<sub>x</sub> core-  
260 shell nanoparticle sample. This result could be explained by the synthesis process in which the  
261 FeO<sub>x</sub> nanoparticles from the same synthesis were used as seeds for core-shell nanoparticle  
262 growth. Even though the FeO<sub>x</sub>-NiO<sub>x</sub> core-shell nanoparticles were synthesized starting with the  
263 FeO<sub>x</sub> nanoparticles, which would suggest that that Fe K-edge position should also be shifted to  
264 higher eV and match that of the NiO<sub>x</sub>/FeO<sub>x</sub> and FeO<sub>x</sub> samples, the edge is in fact positioned at a  
265 slightly lower eV. This result is consistent with the EELS Fe L<sub>2,3</sub> edge results in **Figure 7** and  
266 suggests that the Fe atoms were in a more electron-rich chemical environment in this sample.  
267 The pre-edge features of all three samples are quite similar in shape and position and align most  
268 closely with the NiFe<sub>2</sub>O<sub>4</sub> pre-edge position, albeit with a lower pre-edge intensity. The lower  
269 pre-edge intensity suggests an octahedral coordination environment, and the lower pre-edge  
270 intensity combined with the lower eV edge position suggest an iron phase that has Fe(II) and  
271 Fe(III) species. While the edge is not shifted fully to the lower eV position of the Fe<sub>3</sub>O<sub>4</sub> reference  
272 material, the slight shift is suggestive of some of the Fe atoms having a lower oxidation state,  
273 similar to that of a Fe<sub>3</sub>O<sub>4</sub>-like phase, perhaps in combination with a Fe<sub>2</sub>O<sub>3</sub>-like phase. The minor  
274 shift suggests a small contribution of more electron-rich Fe atoms to the overall ensemble of Fe  
275 in the nanoparticles.

276 For the  $\text{NiO}_x\text{-NiO}_x/\text{FeO}_x$  core-mixed shell nanoparticle sample, the Fe K-edge spectrum  
277 exhibited features that are quite different from that of  $\text{NiO}_x/\text{FeO}_x$  alloy or  $\text{FeO}_x\text{-NiO}_x$  core-shell  
278 nanoparticles. This result may potentially be in part because the  $\text{Fe}(\text{CO})_5$  precursor was used in  
279 place of  $\text{Fe}(\text{acac})_3$ . However, the result may also be a result of the different core-shell  
280 morphology that was formed and the presence of Fe in the iron oxide shell. The edge peak is  
281 broad and has a decreased intensity, as compared to the other samples. This result suggests a  
282 more disordered structure to the nanoparticles, as well as a population of oxidation states within  
283 the nanoparticle. By comparing with spectra of the standard samples, the Fe in this sample is  
284 likely to be a mixture of 2+/3+ state, which also agrees with the XRD results. The slightly higher  
285 intensity pre-edge suggests a distorted octahedral structure. This change in the pre-edge feature  
286 may be a result of the mixed metal oxide/hydroxide shell, where the presence of both metals in  
287 an oxide/hydroxide phase would likely cause distortions in the coordination chemistry of the Fe.



288  
289

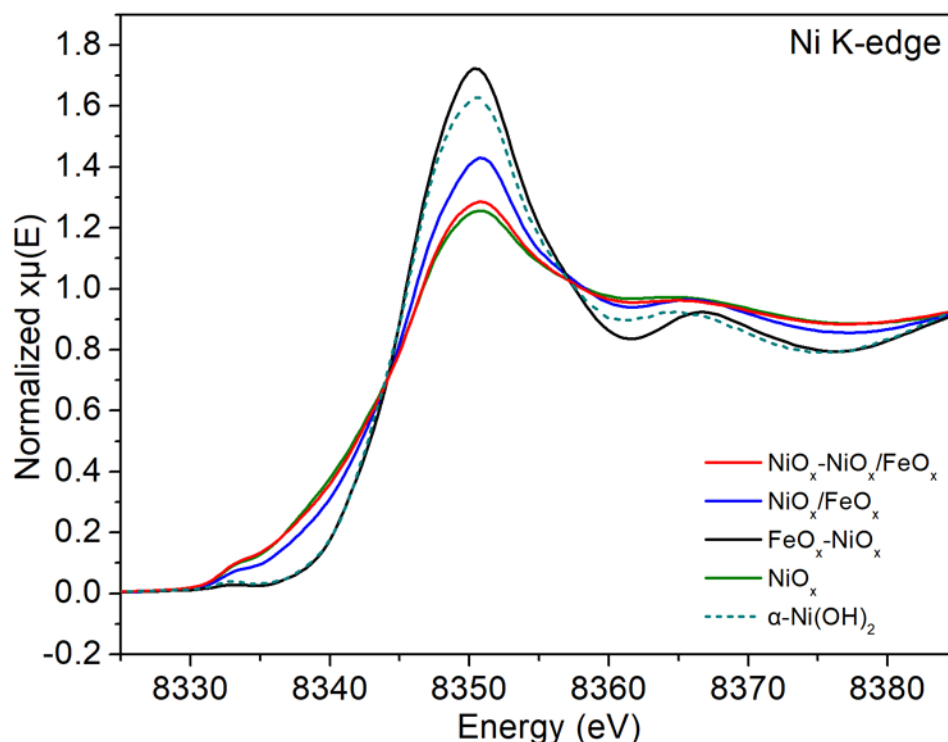


290 **Figure 5.** XAS spectra of Fe K-edge for the nanoparticle catalysts: NiO<sub>x</sub>-NiO<sub>x</sub>/FeO<sub>x</sub> core-mixed  
291 shell (red), NiO<sub>x</sub>/FeO<sub>x</sub> alloy (blue), FeO<sub>x</sub>-NiO<sub>x</sub> core-shell (black), and FeO<sub>x</sub> (pink). The XAS  
292 spectra of selected Fe bulk standards were plotted in dash curves: Fe<sub>3</sub>O<sub>4</sub> (orange), Fe<sub>2</sub>O<sub>3</sub> (dark  
293 yellow), Fe(OH)<sub>3</sub> (wine), and NiFe<sub>2</sub>O<sub>4</sub> (grey).  
294

295 The EXAFS region (**Figure S6**) suggests slight differences in Fe-O bond length in the first  
296 coordination sphere amongst the experimental samples, along with a shoulder around 1 Å, which  
297 is indicative of a contribution from iron hydroxide and similar to EXAFS spectra obtained for the  
298 Fe K edge of other Fe<sub>x</sub>Ni<sub>y</sub>(OH)<sub>z</sub> materials.<sup>36,53</sup> All experimental samples appear to have an Fe-O  
299 bond length that is slightly larger than the most relevant reference material, Fe<sub>3</sub>O<sub>4</sub>, and the NiO<sub>x</sub>-  
300 NiO<sub>x</sub>/FeO<sub>x</sub> core-mixed shell nanoparticle sample resulted in a slightly larger bond length than  
301 the other experimental samples. The second coordination sphere metal-metal distances (Fe-O-  
302 Fe/Ni) also vary as a function of the different experimental samples and as compared to the  
303 reference materials. Generally, there appears to be more variability in the second coordination  
304 sphere than in the first coordination sphere, which may result from the influences of Fe-Ni  
305 substitution and phase structural differences as a result of the different morphologies synthesized  
306 in nanoparticle form. The broad peak obtained for core-shell FeO<sub>x</sub>-NiO<sub>x</sub> is suggestive of the  
307 Fe<sub>3</sub>O<sub>4</sub> reference material spectra,<sup>54-56</sup> with less well-defined peak separation within the second  
308 coordination sphere; this peak splitting is caused by the multiple chemical environments of the  
309 Fe atoms, and thus multiple Fe-O-Fe metal-metal distances, in the Fe<sub>3</sub>O<sub>4</sub> crystal structure,  
310 nominally described as an Fe(II)/Fe(III) mixed oxidation state material. The peak of the second  
311 coordination sphere for FeO<sub>x</sub> vs NiO<sub>x</sub>/FeO<sub>x</sub> is less broad and is positioned at shorter vs longer  
312 radial distance, respectively. The peak of the second coordination sphere for the core-mixed shell  
313 NiO<sub>x</sub>-NiO<sub>x</sub>/FeO<sub>x</sub> has significantly lower peak intensity, suggesting structural disorder. The peak  
314 is also more narrow than those of the other experimental samples and is located at lower radial

315 distance, as compared to NiO<sub>x</sub>/FeO<sub>x</sub>; lower radial distance is suggestive of a compressed Fe-O-M  
316 metal-metal bond distance.

317 The spectra for Ni are plotted in **Figure 6**, supplemented with a full set of Ni standard spectra  
318 plotted in **Figure S7**. The spectral shapes of the Ni K-edge for the NiO<sub>x</sub>-NiO<sub>x</sub>/FeO<sub>x</sub> core-mixed  
319 shell nanoparticles and the NiO<sub>x</sub> nanoparticles had nearly identical features in both the pre-edge  
320 and the white line edge. This result clearly indicates that the majority of the Ni atoms in the  
321 NiO<sub>x</sub>-NiO<sub>x</sub>/FeO<sub>x</sub> core-mixed shell nanoparticles were in a chemical environment like that of the  
322 NiO<sub>x</sub> nanoparticles, which is likely to be  $\alpha$ -Ni(OH)<sub>2</sub>, based on the XRD results. The NiO<sub>x</sub>/FeO<sub>x</sub>  
323 alloy nanoparticles resulted in a pre-edge shape and intensity that was quite similar to the NiO<sub>x</sub>  
324 and NiO<sub>x</sub>-NiO<sub>x</sub>/FeO<sub>x</sub> nanoparticles. All three samples have a pre-edge intensity that is higher  
325 than that of the  $\alpha$ -Ni(OH)<sub>2</sub> reference material, suggesting that the Ni species of these three  
326 samples are in a distorted octahedral coordination geometry, rather than the octahedral geometry  
327 expected for  $\alpha$ -Ni(OH)<sub>2</sub>. In contrast, the pre-edge of the FeO<sub>x</sub>-NiO<sub>x</sub> core-shell nanoparticles  
328 matches the shape and intensity of  $\alpha$ -Ni(OH)<sub>2</sub>, suggesting the Ni atoms are in an octahedral  
329 coordination environment typical of the alpha hydroxide phase. This conclusion is further  
330 supported by the similar white line edge position and peak intensity of the FeO<sub>x</sub>-NiO<sub>x</sub> core-shell  
331 nanoparticles, as compared to the  $\alpha$ -Ni(OH)<sub>2</sub> reference material. Across the set of experimental  
332 samples, all of the samples displayed an edge position indicative of  $\alpha$ -Ni(OH)<sub>2</sub>, and thus, the Ni  
333 was likely in 2+ state.<sup>22</sup>



334

335 **Figure 6.** XAS spectra of Ni K-edge for the nanoparticle catalysts: NiO<sub>x</sub>-NiO<sub>x</sub>/FeO<sub>x</sub> core-mixed  
 336 shell (red), NiO<sub>x</sub>/FeO<sub>x</sub> alloy (blue), FeO<sub>x</sub>-NiO<sub>x</sub> core-shell (black), and NiO<sub>x</sub> (green). The XAS  
 337 spectrum of α-Ni(OH)<sub>2</sub> bulk standard was plotted in a dark green dash curve.

338

339 Similar to the results for the Fe K edge, the EXAFS region (**Figure S8**) suggests slight shifts

340 in Ni-O first coordination sphere bond distances. However, the variability observed in the Fe

341 EXAFS region for the second coordination sphere is not apparent in the Ni EXAFS region for

342 the Ni second coordination sphere (Ni-O-Ni/Fe). This result may suggest that some of the

343 differences observed in nanoparticle structure and, ultimately, electrochemical performance, are

344 a result of differences in the chemical coordination environment of the Fe, more so than the Ni,

345 species in these nanoparticle materials. The shape and peak position of the second coordination

346 sphere is quite similar to that of the α-Ni(OH)<sub>2</sub> reference material for all of the experimental

347 samples.

348 Further analysis of EELS data from individual nanoparticles reveals the differences in local

349 chemical states of Fe and Ni between the core and the shell in the core-shell structures and

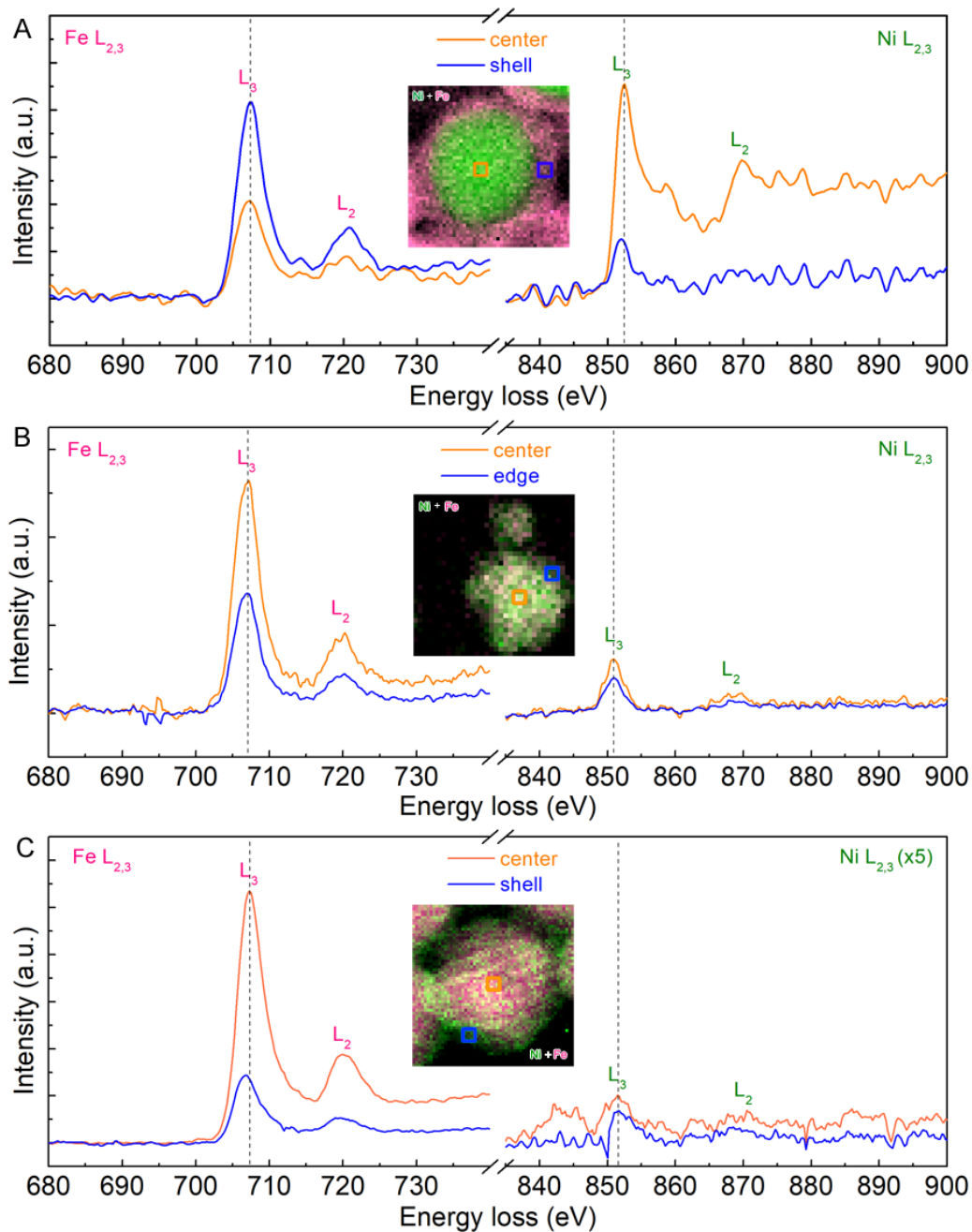
350 provides results that correspond well with XAS data on the bulk samples. **Figure 7** displays the  
351 EELS spectra of the Ni and Fe  $L_{2,3}$ -edges extracted from the center and the edge of the core-shell  
352 nanoparticles (i.e.,  $\text{NiO}_x\text{-NiO}_x/\text{FeO}_x$  core-mixed shell and  $\text{FeO}_x\text{-NiO}_x$  core-shell) and the  
353  $\text{NiO}_x/\text{FeO}_x$  alloy nanoparticle. No peak shifts for both the Fe and Ni  $L_{2,3}$ -edges were found for  
354 the alloy nanoparticles, suggesting the uniform chemical environment of both Fe and Ni across  
355 the nanoparticle, but shifts of the peak positions were observed in the EELS spectra for the core-  
356 shell structures. Based on the shift of the energy onset, the relative oxidation state,<sup>57-58</sup>  
357 coordination environment,<sup>58-60</sup> and electron density of elements in the center and the shell can be  
358 compared. The lower energy onset can correspond to a lower oxidation state or an electron rich  
359 state of the element due to the screening effect of outer-shell electrons.<sup>61-62</sup> For iron, a shift to  
360 lower energy onset may also suggest a shift in coordination from octahedral to tetrahedral. The  
361 direct comparison of the core and shell energy onset, however, is not straightforward because  
362 TEM is a 2-D projection of an object and thus each center spectrum contains the information of  
363 both the core and shell. Nonetheless, comparing the center and shell spectra, the energy shifts  
364 could provide evidence for local chemical environment changes of elements.

365 For  $\text{NiO}_x\text{-NiO}_x/\text{FeO}_x$  core-mixed shell nanoparticles, the energy positions of the Fe  $L_{2,3}$ -  
366 edges in the center and shell spectra are essentially the same because there is no Fe in the core  
367 and both spectra indicate the Fe in the shell. For Ni, however, the energy onset of the  $L_3$  edge in  
368 the shell is 0.5 eV lower than that in the center. Although the center spectrum contains the Ni  
369 signal from both the core and the shell, most of the Ni signal is contributed from the pure Ni core  
370 because the shell is very thin, with a thickness that is  $1/8^{\text{th}}$  of the core diameter, and is composed  
371 of a mixture of Ni and Fe at an atomic ratio of 0.39/1. Prior work has shown that a shift to lower  
372 eV can be due to the presence of nickel metal rather than nickel oxide.<sup>58</sup> However, research has

373 also shown that when metal atoms are incorporated into a nanostructured material,  $L_{2,3}$  edge  
374 shifts may also occur and are thought, generally, to result from shifts in bi-metallic influences on  
375 coordination<sup>60</sup> and spin state.<sup>63</sup> It is unlikely that the Ni atoms in the shell of these nanoparticles  
376 experienced a full oxidation state change from  $Ni^{2+}$  to  $Ni^0$ ; however, the Fe atoms present in the  
377 shell can contribute electron density to the Ni atoms. Thus, we might interpret the onset energy  
378 shift of the Ni in the shell as likely due to the contributions of electron transfer from surrounding  
379 Fe in the shell, which provide electron-rich Ni on the surface of the  $NiO_x$ - $NiO_x/FeO_x$  core-mixed  
380 shell nanoparticles. This shift could also be a result of the strain effects; however, further  
381 analysis of the crystal structure difference at the core-shell interface is needed in order to  
382 determine the strain states.<sup>64</sup> Additional evidence for the proposed electron transfer or electron  
383 donation from Fe to Ni is supported by the Fe K edge EXAFS, where the smaller radial distance  
384 of the second coordination sphere suggests a compressed Fe-O-M bond distance and loss of  
385 electron density, along with the XPS results as shown in **Figure S2**. The binding energy of Fe 2p  
386 electrons for  $NiO_x$ - $NiO_x/FeO_x$  increased by 0.8 eV compared to that for  $FeO_x$  while the binding  
387 energy of Ni 2p electrons for  $NiO_x$ - $NiO_x/FeO_x$  decreased by 0.2 eV compared to that for  $NiO_x$ .  
388 These corroborative results suggest that electrons are preferentially transferred or donated from  
389 Fe to Ni in the shell of the  $NiO_x$ - $NiO_x/FeO_x$  core-mixed shell nanostructures.

390 In contrast, for the  $FeO_x$ - $NiO_x$  core-shell nanoparticles, no difference was observed in the  
391 peak position of the Ni  $L_3$ -edge in EELS spectra while a 0.5 eV shift to lower energy for the peak  
392 position of the Fe  $L_3$ -edge was observed in the shell spectrum compared to the center spectrum.  
393 The shift to lower energy suggests the presence of Fe(II) species, which is supported by our  
394 previous analysis of the Fe K-edge spectra. This energy onset decrease in eV for the Fe at the  
395 interface of the core-shell nanoparticles could be attributed to the deposition of metallic Ni from

396 the thermal decomposition of the Ni(0) organometallic complex thermal deposition, leading to an  
397 electron-rich environment for the surface Fe. The XPS data also indicates that Ni is more  
398 electron-rich in FeO<sub>x</sub>-NiO<sub>x</sub> core-shell nanoparticles than in NiO<sub>x</sub> nanoparticles, which is likely  
399 due to the use of precursors with different valence (Ni<sup>0</sup> versus Ni<sup>2+</sup>) in the corresponding  
400 synthesis. This result is consistent with XAS results that the Fe K edge of FeO<sub>x</sub>-NiO<sub>x</sub> core-shell  
401 is in fact positioned at a lower eV compared to FeO<sub>x</sub>.



402

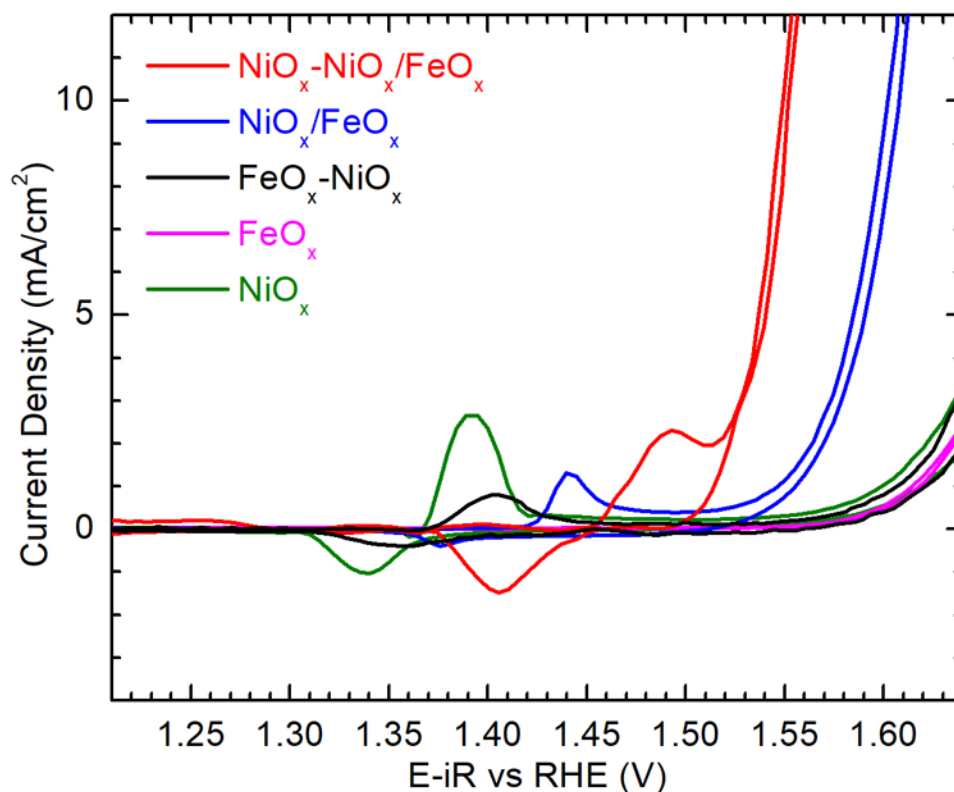
403 **Figure 7.** EELS spectra of Ni and Fe  $L_{2,3}$ -edges extracted from the center region (orange box)  
 404 and the shell region (blue box) of each nanoparticle displayed in the inset of each panel: (A)  
 405  $\text{NiO}_x\text{-NiO}_x/\text{FeO}_x$  core-mixed shell nanoparticle showing that the energy positions of the Fe  $L_{2,3}$ -  
 406 edges in the center and shell spectra were essentially the same while the energy onset of the Ni  
 407  $L_3$  edge in the shell was 0.5 eV lower than that in the center. (B)  $\text{NiO}_x/\text{FeO}_x$  alloy nanoparticle  
 408 indicating no peak shifts for both the Fe and Ni  $L_{2,3}$ -edges. (C)  $\text{FeO}_x\text{-NiO}_x$  core-shell  
 409 nanoparticle showing that no difference was observed in the peak position of the Ni  $L_3$ -edge  
 410 while a 0.5 eV shift to lower energy for the peak position of the Fe  $L_3$ -edge was observed in the  
 411 shell spectrum compared to the center spectrum.

412

413 The three different morphologies of Ni-Fe-based nanostructures (i.e., NiO<sub>x</sub>-NiO<sub>x</sub>/FeO<sub>x</sub> core-  
414 mixed shell, NiO<sub>x</sub>-FeO<sub>x</sub> alloy, and FeO<sub>x</sub>-NiO<sub>x</sub> core-shell) along with the controls (i.e., NiO<sub>x</sub> and  
415 FeO<sub>x</sub>) were evaluated for OER. The OER activity of the nanoparticles was assessed by their  
416 cyclic voltammetry (CV) profile in 1 M KOH. **Figure 8** shows the CV profile comparison of  
417 these nanocatalysts. The NiO<sub>x</sub>-NiO<sub>x</sub>/FeO<sub>x</sub> core-mixed shell nanoparticles exhibited the best  
418 performance with the lowest onset potential, which reached the benchmark current density of 10  
419 mA/cm<sup>2</sup> at 1.55 V vs RHE. Switching another water-soluble surface ligand such as PEG-NH<sub>2</sub>  
420 increased the onset potential by 60 mV (**Figure S9**). The NiO<sub>x</sub>-FeO<sub>x</sub> alloy nanoparticles had the  
421 second lowest onset potential and reached 10 mA/cm<sup>2</sup> at 1.60 V vs RHE. The remaining  
422 nanocatalysts were rather poor OER electrocatalysts, showing much higher onset potentials. The  
423 two bimetallic nanocatalysts (i.e., NiO<sub>x</sub>-NiO<sub>x</sub>/FeO<sub>x</sub> core-mixed shell and NiO<sub>x</sub>/FeO<sub>x</sub> alloy)  
424 drastically outperformed the two monometallic nanocatalysts (i.e. NiO<sub>x</sub> or FeO<sub>x</sub> alone), which  
425 agrees with the literature reported on the thin film studies.<sup>19, 22, 36, 65</sup> Another bimetallic  
426 nanocatalyst (FeO<sub>x</sub>-NiO<sub>x</sub> core-shell) did not improve the onset potential compared to NiO<sub>x</sub> or  
427 FeO<sub>x</sub>, suggesting that the 3-D morphology has a significant influence on the electrocatalytic  
428 activity of the NiFe-based nanocatalysts. This result is also likely driven by the composition of  
429 the iron and nickel at the surface of the nanoparticles, where the atomic composition of Ni in the  
430 FeO<sub>x</sub>-NiO<sub>x</sub> core-shell nanoparticles was quite low (7.2%). We expect, based on prior  
431 literature,<sup>19, 22, 29, 36, 65-66</sup> that an Fe/Ni atomic ratio in the range of 20-80 to 50-50 will be the most  
432 active for OER. Interestingly, the NiO<sub>x</sub>/FeO<sub>x</sub> alloy nanoparticles fit this parameter range, but the  
433 NiO<sub>x</sub>-NiO<sub>x</sub>/FeO<sub>x</sub> core-mixed shell nanoparticles do not fit this expectation, based on our  
434 compositional analysis from EELS. We thus attribute the OER activity of the NiO<sub>x</sub>-NiO<sub>x</sub>/FeO<sub>x</sub>  
435 nanoparticles to the modified electronic structure of the Fe and Ni atoms in the mixed metal shell,



436 where it appears from EELS and XPS analysis that the Ni atoms are more electron rich, while the  
 437 Fe atoms likely are donating electrons to the Ni atoms.



438  
 439  
 440 **Figure 8.** CV profiles of the nanoparticle catalysts obtained in 1 M KOH at a scan rate of 10  
 441 mV/s: NiO<sub>x</sub>-NiO<sub>x</sub>/FeO<sub>x</sub> core-mixed shell (red), NiO<sub>x</sub>/FeO<sub>x</sub> alloy (blue), FeO<sub>x</sub>-NiO<sub>x</sub> core-shell  
 442 (black), FeO<sub>x</sub> (pink), and NiO<sub>x</sub> (green).

443  
 444 The difference in 3-D morphology of these nanocatalysts also impacts the characteristic Ni  
 445 redox peak in the region of 1.30 – 1.53 V of CV profiles. The NiO<sub>x</sub> nanoparticles exhibited the  
 446 largest area for the Ni redox peaks, which occurred at the lowest potential among all the  
 447 nanocatalysts. As can be seen from the CV data, the height of the Ni redox peak does not  
 448 necessarily correlate directly with OER activity; NiO<sub>x</sub> alone is expected to have a distinct redox  
 449 peak but low OER activity in purified alkaline electrolyte, as there are no Fe atoms present to  
 450 enhance the OER reaction. The FeO<sub>x</sub>-NiO<sub>x</sub> core-shell nanocatalyst has a small characteristic Ni  
 451 redox peak despite the presence of Ni; this small peak is likely an indication of the low Ni

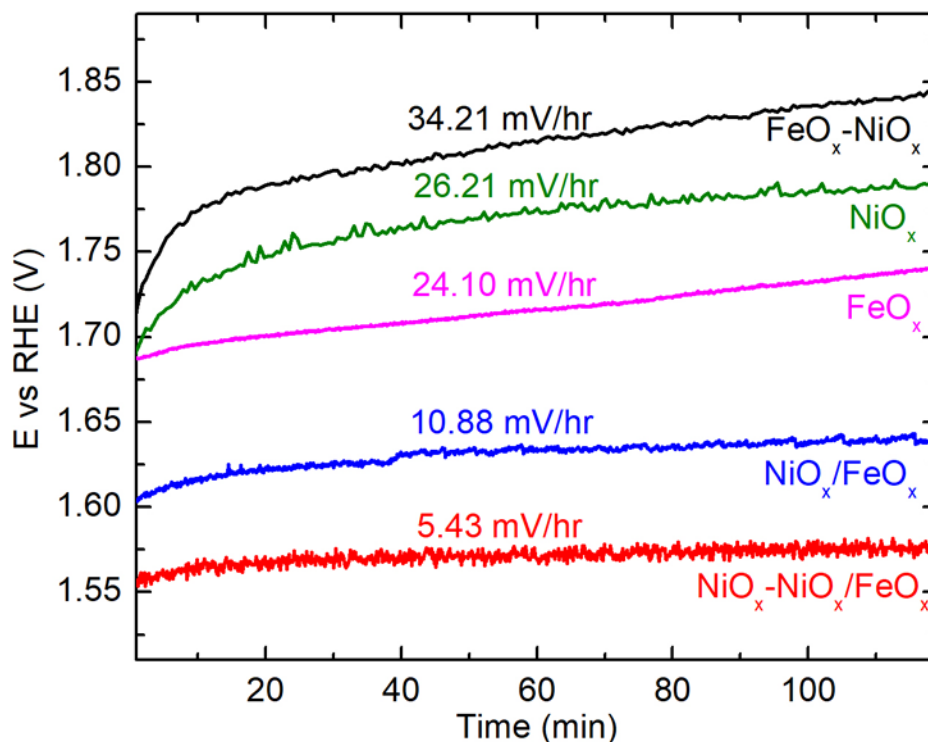
452 content in these core-shell nanoparticles. NiO<sub>x</sub>/FeO<sub>x</sub> alloy nanoparticles had the second largest  
453 area for the Ni redox peak and a slight shift to higher voltage of the potential compared to NiO<sub>x</sub>  
454 nanoparticles. Unlike NiO<sub>x</sub> and NiO<sub>x</sub>/FeO<sub>x</sub> alloy nanoparticles, the NiO<sub>x</sub>-NiO<sub>x</sub>/FeO<sub>x</sub> core-mixed  
455 shell nanoparticles had the highest voltage onset for the Ni redox peak, immediately before the  
456 onset potential of OER. The overall trend for the change of the characteristic Ni redox peaks  
457 agrees with previous studies,<sup>19, 65</sup> which concluded that incorporation of Fe in NiO<sub>x</sub> thin films  
458 increases the Ni redox potential and decreases the area of the Ni redox peaks. Further analysis  
459 was performed to calculate the turnover frequency (TOF) based on the quantitative Ni in the  
460 samples, where the amount of Ni was estimated based on either the ICP-MS results or the  
461 integration of the redox wave (i.e., anodic wave) for each of the nanocatalysts. The TOF values  
462 for different nanocatalysts are listed in **Table S2**. For TOF<sub>ICP-MS</sub>, the NiO<sub>x</sub>-NiO<sub>x</sub>/FeO<sub>x</sub> core-  
463 mixed shell had the highest value of 1.175 s<sup>-1</sup>, followed by NiO<sub>x</sub>/FeO<sub>x</sub> alloy with a value of  
464 0.090 s<sup>-1</sup>. The TOF<sub>ICP-MS</sub> values for NiO<sub>x</sub> and FeO<sub>x</sub>-NiO<sub>x</sub> were 60-80 times lower at 0.006 s<sup>-1</sup> and  
465 0.003 s<sup>-1</sup>, respectively. The TOF<sub>redox wave</sub> was also calculated with the assumptions of either 1  
466 electron or 1.5 electron transfer per Ni atom.<sup>67</sup> The TOF<sub>redox wave</sub> values for all of the  
467 nanocatalysts were 2-5 times higher than those of the corresponding TOF<sub>ICP-MS</sub>; however, the  
468 trend of both TOF values appeared to be the same in order of decreasing activity, with NiO<sub>x</sub>-  
469 NiO<sub>x</sub>/FeO<sub>x</sub> core-mixed shell > NiO<sub>x</sub>/FeO<sub>x</sub> alloy > NiO<sub>x</sub> ~ FeO<sub>x</sub>-NiO<sub>x</sub>. The TOF values agreed  
470 well with the OER activity assessed based on the onset potential of the benchmark current  
471 density of 10 mA/cm<sup>2</sup>.

472 In addition to the electrocatalytic activity, the stability of the nanocatalysts was measured by  
473 chronopotentiometry (CP) for 2 h in 1 M KOH, as shown in **Figure 9**. The degradation rate was  
474 calculated by taking the slope of potential over time for each curve corresponding to each

475 nanocatalyst. The  $\text{NiO}_x\text{-NiO}_x/\text{FeO}_x$  core-mixed shell nanoparticles had the lowest degradation  
476 rate of 5.4 mV/h, followed by  $\text{NiO}_x/\text{FeO}_x$  alloy nanoparticles at a rate of 10.9 mV/h. The  $\text{FeO}_x$ ,  
477  $\text{NiO}_x$ , and  $\text{FeO}_x\text{-NiO}_x$  had faster degradation rates at 24.1, 26.2, and 34.2 mV/h, respectively.  
478 The most active nanocatalyst (i.e.  $\text{NiO}_x\text{-NiO}_x/\text{FeO}_x$  core-mixed shell nanoparticles) was found to  
479 be the most stable electrocatalyst in this series. The  $\text{NiO}_x/\text{FeO}_x$  alloy was the second best  
480 electrocatalyst based on the assessment of both activity and stability. The  $\text{NiO}_x/\text{FeO}_x$  alloy  
481 nanoparticles has a mixed molar composition of  $\sim 0.8:1$  (Ni:Fe) while the  $\text{NiO}_x\text{-NiO}_x/\text{FeO}_x$  core-  
482 mixed shell nanoparticles contains a pure  $\text{NiO}_x$  core and  $\sim 0.4:1$  (Ni:Fe) mixed alloy shell, but the  
483  $\text{FeO}_x\text{-NiO}_x$  core-shell appeared to be a pure  $\text{NiO}_x$  cluster shell (i.e., without any Fe included in  
484 the  $\text{NiO}_x$  structure). To our surprise, the  $\text{NiO}_x\text{-NiO}_x/\text{FeO}_x$  core-mixed shell nanoparticles, with  
485 half the amount of Ni in the shell compared to the  $\text{NiO}_x/\text{FeO}_x$  alloy nanoparticles, out-performed  
486 the  $\text{NiO}_x/\text{FeO}_x$  alloy nanoparticles in both activity and stability. Further adding a pure  $\text{FeO}_x$  shell  
487 increased the onset potential by 100 mV and thus reduced the electrocatalytic activity (**Figure**  
488 **S10**); and the  $\text{FeO}_x$  core- $\text{NiO}_x/\text{FeO}_x$  mixed shell has similar activity as the  $\text{NiO}_x/\text{FeO}_x$  alloy with  
489 an onset potential at 1.64 V (**Figure S11**). These results suggest that the mixed  $\text{NiO}_x/\text{FeO}_x$  alloy  
490 composition is important to achieve high electrocatalytic activity for OER and the 3-D  
491 morphology plays a key role in optimization of the electrocatalytic activity and stability of the  
492 nanocatalyst for OER.

493

494



495  
496  
497 **Figure 9.** Chronopotentiometry (CP) of the nanocatalysts obtained in 1 M KOH at a current  
498 density of 10 mA/cm<sup>2</sup> for 2 h: NiO<sub>x</sub>-NiO<sub>x</sub>/FeO<sub>x</sub> core-mixed shell (red), NiO<sub>x</sub>/FeO<sub>x</sub> alloy (blue),  
499 FeO<sub>x</sub>-NiO<sub>x</sub> core-shell (black), FeO<sub>x</sub> (pink), and NiO<sub>x</sub> (green).

500  
501 **Conclusion**

502 In this study, we developed a scalable, oil-based synthesis based on thermal decomposition  
503 of organometallic complexes that could manipulate both the morphology and crystalline phase of  
504 the Ni-Fe-based nanocatalysts. Highly uniform Ni-Fe-based nanostructures with different  
505 morphologies (i.e., Ni-Fe core-shell, Ni/Fe alloy, and Fe-Ni core-shell) were synthesized *via*  
506 either sequential or simultaneous injection. TEM imaging revealed that the Ni-Fe core-shell was  
507 more complex due to the diffusion of Ni into the Fe shell, while the Ni-Fe alloy nanoparticle  
508 structure appeared to be a homogeneous mixture and the Fe-Ni core-shell structure contained an  
509 FeO<sub>x</sub> core with NiO<sub>x</sub> islands/thin shell. Coupled with x-ray characterization methods on the bulk  
510 and surface of the sample, we elucidate the morphology, composition, and structure of individual  
511 particles for each of these nanostructures to be NiO<sub>x</sub>-NiO<sub>x</sub>/FeO<sub>x</sub> core-mixed shell, NiO<sub>x</sub>/FeO<sub>x</sub>

512 alloy, and FeO<sub>x</sub>-NiO<sub>x</sub> core-shell structures. The overpotentials of these nanocatalysts increased  
513 in the order of NiO<sub>x</sub>-NiO<sub>x</sub>/FeO<sub>x</sub> core-mixed shell < NiO<sub>x</sub>/FeO<sub>x</sub> alloy < FeO<sub>x</sub>-NiO<sub>x</sub> core-shell  
514 structures  $\approx$  NiO<sub>x</sub>  $\approx$  FeO<sub>x</sub>. The TOF values obtained based on both ICP-MS and redox wave  
515 followed the same trend. These results suggested that the crystalline FeO<sub>x</sub> core did not promote  
516 the catalytic activity of NiO<sub>x</sub> in the FeO<sub>x</sub>-NiO<sub>x</sub> core-shell morphology, possibly due to the high  
517 crystallinity of FeO<sub>x</sub>, which prevented Fe diffusion into the NiO<sub>x</sub> shell. In contrast, the  
518 amorphous, disordered nature of the NiO<sub>x</sub> core, which appears to be most similar to  $\alpha$ -Ni(OH)<sub>2</sub>,  
519 allowed the diffusion of Ni into the FeO<sub>x</sub> for the NiO<sub>x</sub>-NiO<sub>x</sub>/FeO<sub>x</sub> core-mixed shell nanoparticles.  
520 The resultant mixed metal hydroxide/oxide shell enabled the most active and stable nanocatalyst,  
521 which out-performed the comparison NiO<sub>x</sub>/FeO<sub>x</sub> alloy nanoparticles with a 1:1 composition  
522 expected to be active for OER. These findings highlight that not only the crystallinity, but also  
523 the 3-D morphology, phase, and chemical environment of both metal species, disorder, and  
524 composition, can significantly affect the electrocatalytic activity and stability of nanocatalysts for  
525 alkaline OER.

## 526 **Experimental Methods**

527 **Synthesis of NiO<sub>x</sub>-NiO<sub>x</sub>/FeO<sub>x</sub> Core-Mixed Shell Nanoparticles.** The Ni-Fe core-shell  
528 nanoparticles were synthesized by a two-step procedure involving the synthesis of Ni core and  
529 following by coating the Ni core with Fe shell. In a typical synthesis, Ni(acac)<sub>2</sub> (51.5 mg, 0.2  
530 mmol), 4 mL of octadecene (ODE), and 1 mL of oleylamine (OLAM) were added to a 3-neck,  
531 round bottom flask equipped with a condenser and a Schlenk line system. This reaction mixture  
532 was degassed for 10 min before 1mL of trioctylphosphine (TOP) was added to the reaction.  
533 Under the protection of argon, the reaction was heated to 220 ° C within 10 min and was held at  
534 220 ° C for additional 20 min to allow the formation of Ni cores. The reaction was quenched by

535 removing the flask from the heating mantle. After the reaction mixture was cooled to 50 ° C, the  
536 product was transferred to a 50 mL centrifuge tube filled with 5 mL toluene and 20 mL of  
537 ethanol which was centrifuged at 8000 rcf for 5 min to remove excess reactants. The nanoparticle  
538 pellet was dispersed and purified using a mixture of 1:4 toluene and ethanol. The nanoparticles  
539 were dispersed in 6 mL of toluene.

540 For the Fe shelling procedure, 1.8 mL of the above Ni nanoparticles (~5 mg) was dried under  
541 a stream of argon in a 3-neck, round-bottom flask. Then, 200 µL of OLAM and 5 mL of ODE  
542 were added to the flask and the nanoparticles were dispersed in the mixture *via* sonication. To  
543 ensure a uniform coating, the reaction temperature was ramped using a step-wise procedure  
544 during the addition of Fe precursor. The temperature was first ramped to 100 ° C prior to the  
545 degassing of the reaction mixture. The temperature was then continued to ramp to 110 ° C and  
546 held for 10 min. Then, Fe(CO)<sub>5</sub> (20 µL, 0.15 mmol) was injected into the reaction using a gas-  
547 tight syringe. After adding the Fe precursor, the temperature was increased at a rate of 2.5  
548 ° C/min until 200 ° C and the reaction was held at 200 ° C for 60 min. After the reaction was  
549 quenched and cooled to 50 ° C, the product was transferred to a 50 mL centrifuge tube filled  
550 with ethanol to 30 mL which was centrifuged at 8000 rcf for 5 min to remove excess reactants.  
551 The nanoparticle pellet was dispersed and purified using a mixture of 2:1 toluene and ethanol  
552 and collected by centrifuging at 2000 rcf for 10 min. The nanoparticles were dispersed in 2 mL  
553 of toluene.

554 **Synthesis of Ni-Fe Alloyed Nanoparticles.** Similar procedure was applied to the synthesis of  
555 alloyed nanoparticles as that for the Ni core synthesis except equimolar amounts of Ni(acac)<sub>2</sub>  
556 (25.7 mg, 0.1 mmol) and Fe(acac)<sub>3</sub> (26.5 mg, 0.1 mmol) were used in the reaction.

557 **Synthesis of Fe-Ni Core-Shell Nanoparticles.** The Fe-Ni core-shell nanoparticles were  
558 synthesized by a two-step procedure involving the synthesis of Fe core and following by coating  
559 the Fe core with Fe shell. The same reaction set up and heating procedure were used as that for  
560 the Ni-Fe core-shell unless specified. In a typical synthesis, Fe(acac)<sub>2</sub> (530.0 mg, 1.5 mmol), 4  
561 mL of .5 mL of dibenzyl ether (DBE), and 7.5 mL of oleylamine (OLAM) were used in the  
562 reaction. After degassing, the reaction was heated to 280 ° C and held at 280 ° C for 60 min. The  
563 product was distributed in equal volume into two 50 mL centrifuge tubes filled with ethanol to  
564 30 mL which was centrifuged at 2000 rcf for 10 min to remove excess reactants. The  
565 nanoparticle pellet was dispersed and purified using a mixture of 1:10 toluene and ethanol twice  
566 and collected by centrifuging at 8000 rcf for 5 min. The nanoparticles were dispersed in 6 mL of  
567 toluene.

568 For the Ni shelling procedure, 200 µL of the above Fe nanoparticles (~ 5 mg) was dried  
569 under a stream of argon in a 3-neck, round-bottom flask. Then, 200 µL of OLAM and 5 mL of  
570 ODE were added to the flask and the nanoparticles were dispersed in the mixture *via* sonication.  
571 After degassing, Ni-COD (40.0 mg, 0.15 mmol) added in 2 mL of DBE was injected into the  
572 reaction. The reaction temperature was increased at a rate of 2.5 ° C/min to 200 ° C and held at  
573 200 ° C for 60 min. The product was transferred to a 50 mL centrifuge tube filled with ethanol to  
574 30 mL which was centrifuged at 8000 rcf for 5 min to remove excess reactants. The nanoparticle  
575 pellet was dispersed and purified using ethanol and collected by centrifuging at 12500 rcf for 10  
576 min. The nanoparticles were dispersed in 2 mL of toluene.

577 **Nanoparticle Surface Ligand Exchange.** The nanoparticles dispersed in toluene were  
578 transferred into aqueous dispersion by surface ligand exchange process using  
579 methoxypolyethylene glycol carboxylic acid (PEG-COOH, M.W.=5000). In a typical procedure,

580 2 mL of the nanoparticle suspension in toluene was added to 10 mL of 1 mg/mL PEG-COOH  
581 chloroform solution in a 20 mL scintillation vial. The reaction mixture was capped and stirred  
582 overnight. The product was distributed in two 50 mL centrifuge tubes which were filled to 45  
583 mL with hexane and centrifuged at 15,000 rcf for 10 min. The resulting pellet was purified with  
584 ethanol/water and collected by centrifuging at 20,000 rcf for 30 min at 4 ° C. The final product  
585 was dispersed in 500 µL of ethanol/water for quantification and characterization.

586 **Instrumentation.** Low resolution TEM images were captured using a JEOL JEM-1011  
587 microscope with an accelerating voltage of 100 kV. HAADF-STEM images were acquired using  
588 the JEM-ARM200F microscope equipped with cold field emission gun and double aberration  
589 correctors at the accelerating voltage of 200 kV. The inner and outer collection angles for  
590 HAADF images were 67 and 275 mrad, respectively. The spatial resolution of HAADF images  
591 was 0.8 Å. The 2D EELS mapping of Fe L-edge and Ni L-edge was carried out using a Gatan  
592 energy-loss spectrometer at an accelerating voltage of 200 kV and a beam convergence semi-  
593 angle of 21.2 mrad. Dispersion of 0.25 eV/channel was used to simultaneously acquire Fe L-  
594 edge and Ni L-edge, as well as O K-edge. The dual-EELS mode was adopted for the  
595 convenience of correcting zero-loss. The mass concentrations of Ni and Fe were determined  
596 using a Thermo Scientific iCAP Q ICP-MS. XRD patterns were collected on Rigaku Ultima III  
597 X-ray diffractometer in a parallel beam geometry. Copper anode x-ray tube was used as a  
598 radiation source and diffracted beam monochromator was employed to remove fluorescence  
599 background. Samples were deposited on a zero diffraction Silicon plates (MTI Corp., CA) and  
600 data was collected at 0.07 degrees per minute scan rates in two theta range from 20 to 80 degrees  
601 with 0.1 step. The XPS experiments were carried out in an ultrahigh vacuum (UHV) system with  
602 base pressures  $< 5 \times 10^{-9}$  Torr equipped a hemispherical electron energy analyzer (SPECS,



603 PHOIBOS 100) and twin anode X-ray source (SPECS, XR50). Mg  $K_{\alpha}$  (1253.6 eV) radiation was  
604 used at 15 kV and 20 mA. The angle between the analyzer and X-ray source is  $45^{\circ}$  and  
605 photoelectrons were collected along the sample surface normal. The XPS spectra was analyzed  
606 and deconvoluted using Casa XPS software.

607 **X-ray Absorption Spectroscopy.** The XAS of the samples and the standards were performed at  
608 Argonne National Laboratory (APS 12-BM-B). The standards were purchased from commercial  
609 vendors. Standards included nickel foil, nickel oxide, alpha and beta nickel hydroxide, alpha and  
610 gamma nickel oxyhydroxide, iron foil, iron oxides (FeO, Fe<sub>2</sub>O<sub>3</sub>, and Fe<sub>3</sub>O<sub>4</sub>), iron hydroxide, and  
611 iron nickel oxide. Samples and standards were deposited onto the Kapton tape and were sealed  
612 on top by a layer of Kapton tape. Along with the standards and the samples, metal reference foils  
613 for iron and nickel were also ran simultaneously. The data analysis was done through Athena  
614 software. All the standards and the samples were calibrated to the respective metal reference  
615 foils. The measurements were performed at room temperature in transmission mode (or  
616 fluorescence mode with a 13 elements Ge detector). The samples were scanned at the K-edge of  
617 Fe (7112 eV) (150 eV below to 800 eV above) and Ni (8333 eV).

618 **Electrochemical Characterization.** The CV and CP were performed on a Pine WaveNow 50  
619 potentiostat using a 3-electrode cell setup. In this setup, Au electrode (BASi®) was used to  
620 prepare the working electrode while a graphite rod was used as the counter electrode and  
621 Ag/AgCl (kept inside a salt bridge containing 3 M NaCl solution) was used as the reference  
622 electrode. In all experiments, 1 M KOH was used as the electrolyte solution. The KOH  
623 electrolyte was purified using the method reported by Trotochaud *et. al.*<sup>68</sup> Argon gas was  
624 continuously bubbled throughout the experiments to remove oxygen formed in the solution.

625 Catalyst inks were prepared by mixing the nanoparticles with a cationic ionomer at a ratio of  
626 6:1 (g Fe: g ionomer) in ethanol. The ink was subsequently sonicated for 15 min to mix the  
627 nanoparticles and the ionomer homogeneously. Approximately 1  $\mu\text{l}$  of the ink was deposited  
628 onto the electrode surface ( $0.02\text{ cm}^2$ ) using the dropcast method and was allowed to dry in air.  
629 CV was run at a scan rate of 10 mV/s between 0 V to 0.8 V vs Ag/AgCl. The data at 21<sup>st</sup> cycle  
630 was reported. CP was conducted for 2 h at a current density of 10 mA/cm<sup>2</sup>. Potential in reference  
631 to Ag/AgCl was converted into RHE by using the following equation:  $E_{\text{RHE}} = E_{\text{Ag/AgCl}} +$   
632  $0.059 \cdot \text{pH} + E_{\text{Ag/AgCl}}^0$ , where pH is 14 because the measurement was performed in 1 M KOH;  
633  $E_{\text{Ag/AgCl}}^0$  is 0.21 V for the reference electrode of Ag/AgCl in 3 M NaCl. The  $iR_u$  correction was  
634 applied to the CV curves obtained from the measurement where  $i$  stands for the measured current  
635 in unit ampere and  $R_u$  is the value of uncompensated resistance.  $R_u$  was measured using  
636 potentiostatic electrochemical impedance spectroscopy and the  $R_u$  values were taken at a  
637 frequency of 100 KHz. Calculation for overpotential was done by subtracting the theoretical  
638 potential for OER, 1.23 V, from the measured potential vs. RHE. To calculate the current density  
639 ( $j$ , mA/cm<sup>2</sup>), current is normalized to geometric surface area of the Au electrode ( $0.02\text{ cm}^2$ ).  
640 Chronopotentiometry was conducted for 2 h at a current density of 10 mA/cm<sup>2</sup>.

### 641 **Supporting Information**

642 Reaction yield and cost estimations; elemental quantifications using electron microscopy;  
643 calculation of turn over frequency; TEM images of NiO<sub>x</sub> nanoparticles; XPS spectra; TEM  
644 images of FeO<sub>x</sub> nanoparticles; XAS spectra of Fe and Ni standards; EXAFS region of Fe and Ni;  
645 Table of TOF values; CV profiles of NiO<sub>x</sub>-NiO<sub>x</sub>/FeO<sub>x</sub> with PEG-HH<sub>2</sub> ligands, NiO<sub>x</sub>-NiO<sub>x</sub>/FeO<sub>x</sub>-  
646 FeO<sub>x</sub> and FeO<sub>x</sub>-NiO<sub>x</sub>/FeO<sub>x</sub>.

### 647 **Author Contribution**

648 JC and LFG designed the experiments and wrote the manuscript. RHM and CCC synthesized the  
649 nanocatalysts. PA performed the electrochemical measurement. DS, JZ, and YZ carried out the  
650 electron microscopy characterization. BR and SL performed the XAS measurement. XT  
651 conducted the XPS measurement. DN obtained the XRD results. All authors contributed to data  
652 analysis, manuscript preparation and editing.

### 653 **Acknowledgement**

654 We thank Drs. Zhen Wang and Jun Li for the helpful discussion of EELS analysis. JC, LFG,  
655 RHM, and PA gratefully acknowledge funding support from the National Science Foundation  
656 (NSF), Division of Chemical, Bioengineering, Environmental and Transport Systems (CBET)  
657 Catalysis program (Award # 1703827). HRTEM and EELS were carried out at Brookhaven  
658 National Laboratory (BNL) sponsored by the U.S. Department of Energy (DOE) Basic Energy  
659 Sciences (BES) and by the Materials Sciences and Engineering Division under Contract No. DE-  
660 SC0012704. ICP-MS measurements were carried out at the Arkansas Mass Spectrometry facility,  
661 which is supported by the Arkansas Biosciences Institute. XPS and XRD measurements were  
662 performed at the Center for Functional Nanomaterials (CFN), which is a U.S. DOE Office of  
663 Science Facility, at BNL under Contract No. DE-SC0012704. XAS measurements were  
664 performed at the 12-BM beamline at the Advanced Photon Source, a U.S. DOE Office of  
665 Science User Facility operated for the DOE Office of Science by Argonne National Laboratory  
666 under Contract DE-AC02-06CH11357.

667

668

669 **References**

- 670 1. Zeng, K.; Zhang, D., Recent progress in alkaline water electrolysis for hydrogen production  
671 and applications. *Progress in Energy and Combustion Science* **2010**, *36* (3), 307-326.
- 672 2. Carmo, M.; Fritz, D. L.; Mergel, J.; Stolten, D., A comprehensive review on PEM water  
673 electrolysis. *International Journal of Hydrogen Energy* **2013**, *38* (12), 4901-4934.
- 674 3. Reier, T.; Nong, H. N.; Teschner, D.; Schlögl, R.; Strasser, P., Electrocatalytic Oxygen  
675 Evolution Reaction in Acidic Environments – Reaction Mechanisms and Catalysts. *Advanced*  
676 *Energy Materials* **2017**, *7* (1), 1601275-n/a.
- 677 4. Ma, Z.; Zhang, Y.; Liu, S.; Xu, W.; Wu, L.; Hsieh, Y.-C.; Liu, P.; Zhu, Y.; Sasaki, K.;  
678 Renner, J. N.; Ayers, K. E.; Adzic, R. R.; Wang, J. X., Reaction mechanism for oxygen  
679 evolution on RuO<sub>2</sub>, IrO<sub>2</sub>, and RuO<sub>2</sub>@IrO<sub>2</sub> core-shell nanocatalysts. *Journal of*  
680 *Electroanalytical Chemistry* **2018**, *819*, 296-305.
- 681 5. Reier, T.; Oezaslan, M.; Strasser, P., Electrocatalytic Oxygen Evolution Reaction (OER) on  
682 Ru, Ir, and Pt Catalysts: A Comparative Study of Nanoparticles and Bulk Materials. *ACS*  
683 *Catal.* **2012**, *2* (8), 1765-1772.
- 684 6. Lee, Y.; Suntivich, J.; May, K. J.; Perry, E. E.; Shao-Horn, Y., Synthesis and Activities of  
685 Rutile IrO<sub>2</sub> and RuO<sub>2</sub> Nanoparticles for Oxygen Evolution in Acid and Alkaline Solutions.  
686 *The Journal of Physical Chemistry Letters* **2012**, *3* (3), 399-404.
- 687 7. McCrory, C. C.; Jung, S.; Peters, J. C.; Jaramillo, T. F., Benchmarking heterogeneous  
688 electrocatalysts for the oxygen evolution reaction. *Journal of the American Chemical Society*  
689 **2013**, *135* (45), 16977-16987.
- 690 8. Matsumoto, Y.; Sato, E., Electrocatalytic properties of transition metal oxides for oxygen  
691 evolution reaction. *Materials Chemistry and Physics* **1986**, *14* (5), 397-426.
- 692 9. Man, I. C.; Su, H.-Y.; Calle-Vallejo, F.; Hansen, H. A.; Martínez, J. I.; Inoglu, N. G.; Kitchin,  
693 J.; Jaramillo, T. F.; Nørskov, J. K.; Rossmeisl, J., Universality in Oxygen Evolution  
694 Electrocatalysis on Oxide Surfaces. *ChemCatChem* **2011**, *3* (7), 1159-1165.
- 695 10. Burke, M. S.; Enman, L. J.; Batchellor, A. S.; Zou, S.; Boettcher, S. W., Oxygen Evolution  
696 Reaction Electrocatalysis on Transition Metal Oxides and (Oxy)hydroxides: Activity Trends  
697 and Design Principles. *Chemistry of Materials* **2015**, *27* (22), 7549-7558.
- 698 11. Fabbri, E.; Habereder, A.; Waltar, K.; Kötz, R.; Schmidt, T. J., Developments and  
699 perspectives of oxide-based catalysts for the oxygen evolution reaction. *Catalysis Science &*  
700 *Technology* **2014**, *4* (11), 3800-3821.
- 701 12. Kim, J. S.; Kim, B.; Kim, H.; Kang, K., Recent Progress on Multimetal Oxide Catalysts for  
702 the Oxygen Evolution Reaction. *Advanced Energy Materials* **2018**, *8* (11), 1702774.
- 703 13. Burke, M. S.; Zou, S.; Enman, L. J.; Kellon, J. E.; Gabor, C. A.; Pledger, E.; Boettcher, S. W.,  
704 Revised Oxygen Evolution Reaction Activity Trends for First-Row Transition-Metal  
705 (Oxy)hydroxides in Alkaline Media. *The Journal of Physical Chemistry Letters* **2015**, *6* (18),  
706 3737-3742.
- 707 14. Gong, M.; Dai, H., A mini review of NiFe-based materials as highly active oxygen evolution  
708 reaction electrocatalysts. *Nano Res.* **2015**, *8* (1), 23-39.
- 709 15. Dionigi, F.; Strasser, P., NiFe-Based (Oxy)hydroxide Catalysts for Oxygen Evolution  
710 Reaction in Non-Acidic Electrolytes. *Advanced Energy Materials* **2016**, *6* (23), 1600621.
- 711 16. Tichenor, R. L., Nickel Oxides-Relation Between Electrochemical and Foreign Ion Content.  
712 *Industrial & Engineering Chemistry* **1952**, *44* (5), 973-977.

- 713 17. Młynarek, G.; Paszkiewicz, M.; Radniecka, A., The effect of ferric ions on the behaviour of a  
714 nickelous hydroxide electrode. *Journal of applied electrochemistry* **1984**, *14* (2), 145-149.
- 715 18. Corrigan, D. A., The catalysis of the oxygen evolution reaction by iron impurities in thin-film  
716 nickel-oxide electrodes. *Journal of the Electrochemical Society* **1987**, *134* (2), 377-384.
- 717 19. Trotochaud, L.; Young, S. L.; Ranney, J. K.; Boettcher, S. W., Nickel-iron oxyhydroxide  
718 oxygen-evolution electrocatalysts: The role of intentional and incidental iron incorporation. *J.*  
719 *Am. Chem. Soc.* **2014**, *136*, 6744-6753.
- 720 20. Klaus, S.; Louie, M. W.; Trotochaud, L.; Bell, A. T., Role of Catalyst Preparation on the  
721 Electrocatalytic Activity of Ni<sub>1-x</sub>Fe<sub>x</sub>OOH for the Oxygen Evolution Reaction. *The Journal*  
722 *of Physical Chemistry C* **2015**, *119* (32), 18303-18316.
- 723 21. Ahn, H. S.; Bard, A. J., Surface Interrogation Scanning Electrochemical Microscopy of Ni<sub>1-</sub>  
724 <sub>x</sub>Fe<sub>x</sub>OOH (0 < x < 0.27) Oxygen Evolving Catalyst: Kinetics of the “fast” Iron Sites. *Journal*  
725 *of the American Chemical Society* **2016**, *138* (1), 313-318.
- 726 22. Görlin, M.; Chernev, P.; Ferreira de Araújo, J.; Reier, T.; Dresp, S.; Paul, B.; Krähnert, R.;  
727 Dau, H.; Strasser, P., Oxygen Evolution Reaction Dynamics, Faradaic Charge Efficiency,  
728 and the Active Metal Redox States of Ni-Fe Oxide Water Splitting Electrocatalysts. *Journal*  
729 *of the American Chemical Society* **2016**, *138* (17), 5603-5614.
- 730 23. Görlin, M.; Ferreira de Araújo, J.; Schmies, H.; Bernsmeier, D.; Dresp, S.; Gliech, M.; Jusys,  
731 Z.; Chernev, P.; Kraehnert, R.; Dau, H.; Strasser, P., Tracking Catalyst Redox States and  
732 Reaction Dynamics in Ni-Fe Oxyhydroxide Oxygen Evolution Reaction Electrocatalysts:  
733 The Role of Catalyst Support and Electrolyte pH. *Journal of the American Chemical Society*  
734 **2017**, *139* (5), 2070-2082.
- 735 24. Li, N.; Bediako, D. K.; Hadt, R. G.; Hayes, D.; Kempa, T. J.; von Cube, F.; Bell, D. C.; Chen,  
736 L. X.; Nocera, D. G., Influence of iron doping on tetravalent nickel content in catalytic  
737 oxygen evolving films. *Proceedings of the National Academy of Sciences* **2017**, *114* (7),  
738 1486-1491.
- 739 25. Stevens, M. B.; Trang, C. D. M.; Enman, L. J.; Deng, J.; Boettcher, S. W., Reactive Fe-Sites  
740 in Ni/Fe (Oxy)hydroxide Are Responsible for Exceptional Oxygen Electrocatalysis Activity.  
741 *Journal of the American Chemical Society* **2017**, *139* (33), 11361-11364.
- 742 26. Corrigan, D. A.; Conell, R. S.; Fierro, C. A.; Scherson, D. A., In-situ Moessbauer study of  
743 redox processes in a composite hydroxide of iron and nickel. *The Journal of Physical*  
744 *Chemistry* **1987**, *91* (19), 5009-5011.
- 745 27. Guerlou- Demourgues, L.; Fournès, L.; Delmas, C., In Situ <sup>57</sup>Fe Mössbauer Spectroscopy  
746 Study of the Electrochemical Behavior of an Iron- Substituted Nickel Hydroxide Electrode.  
747 *Journal of The Electrochemical Society* **1996**, *143* (10), 3083-3088.
- 748 28. Chen, J. Y. C.; Dang, L.; Liang, H.; Bi, W.; Gerken, J. B.; Jin, S.; Alp, E. E.; Stahl, S. S.,  
749 Operando Analysis of NiFe and Fe Oxyhydroxide Electrocatalysts for Water Oxidation:  
750 Detection of Fe<sup>4+</sup> by Mössbauer Spectroscopy. *Journal of the American Chemical Society*  
751 **2015**, *137* (48), 15090-15093.
- 752 29. Louie, M. W.; Bell, A. T., An investigation of thin-film Ni-Fe oxide catalysts for the  
753 electrochemical evolution of oxygen. *Journal of the American Chemical Society* **2013**, *135*  
754 (33), 12329-12337.
- 755 30. Klaus, S.; Cai, Y.; Louie, M. W.; Trotochaud, L.; Bell, A. T., Effects of Fe Electrolyte  
756 Impurities on Ni(OH)<sub>2</sub>/NiOOH Structure and Oxygen Evolution Activity. *The Journal of*  
757 *Physical Chemistry C* **2015**, *119* (13), 7243-7254.

- 758 31. Steimecke, M.; Seiffarth, G.; Bron, M., In Situ Characterization of Ni and Ni/Fe Thin Film  
759 Electrodes for Oxygen Evolution in Alkaline Media by a Raman-Coupled Scanning  
760 Electrochemical Microscope Setup. *Analytical Chemistry* **2017**, *89* (20), 10679-10686.
- 761 32. Kim, S.; Tryk, D. A.; Antonio, M. R.; Carr, R.; Scherson, D., In situ x-ray absorption fine  
762 structure studies of foreign metal ions in nickel hydrous oxide electrodes in alkaline  
763 electrolytes. *The Journal of Physical Chemistry* **1994**, *98* (40), 10269-10276.
- 764 33. Balasubramanian, M.; Melendres, C. A.; Mini, S., X-ray Absorption Spectroscopy Studies of  
765 the Local Atomic and Electronic Structure of Iron Incorporated into Electrodeposited  
766 Hydrous Nickel Oxide Films. *The Journal of Physical Chemistry B* **2000**, *104* (18), 4300-  
767 4306.
- 768 34. Landon, J.; Demeter, E.; İnoğlu, N.; Keturakis, C.; Wachs, I. E.; Vasić, R.; Frenkel, A. I.;  
769 Kitchin, J. R., Spectroscopic Characterization of Mixed Fe–Ni Oxide Electrocatalysts for the  
770 Oxygen Evolution Reaction in Alkaline Electrolytes. *ACS Catal.* **2012**, *2* (8), 1793-1801.
- 771 35. Trześniewski, B. J.; Diaz-Morales, O.; Vermaas, D. A.; Longo, A.; Bras, W.; Koper, M. T.  
772 M.; Smith, W. A., In Situ Observation of Active Oxygen Species in Fe-Containing Ni-Based  
773 Oxygen Evolution Catalysts: The Effect of pH on Electrochemical Activity. *Journal of the*  
774 *American Chemical Society* **2015**, *137* (48), 15112-15121.
- 775 36. Friebel, D.; Louie, M. W.; Bajdich, M.; Sanwald, K. E.; Cai, Y.; Wise, A. M.; Cheng, M.-J.;  
776 Sokaras, D.; Weng, T.-C.; Alonso-Mori, R.; Davis, R. C.; Bargar, J. R.; Nørskov, J. K.;  
777 Nilsson, A.; Bell, A. T., Identification of Highly Active Fe Sites in (Ni,Fe)OOH for  
778 Electrocatalytic Water Splitting. *Journal of the American Chemical Society* **2015**, *137* (3),  
779 1305-1313.
- 780 37. Bates, M. K.; Jia, Q.; Doan, H.; Liang, W.; Mukerjee, S., Charge-Transfer Effects in Ni–Fe  
781 and Ni–Fe–Co Mixed-Metal Oxides for the Alkaline Oxygen Evolution Reaction. *ACS Catal.*  
782 **2016**, *6* (1), 155-161.
- 783 38. González-Flores, D.; Klingan, K.; Chernev, P.; Loos, S.; Mohammadi, M. R.; Pasquini, C.;  
784 Kubella, P.; Zaharieva, I.; Smith, R. D.; Dau, H., Nickel-iron catalysts for electrochemical  
785 water oxidation–redox synergism investigated by in situ X-ray spectroscopy with millisecond  
786 time resolution. *Sustainable Energy & Fuels* **2018**.
- 787 39. Smith, R. D.; Pasquini, C.; Loos, S.; Chernev, P.; Klingan, K.; Kubella, P.; Mohammadi, M.  
788 R.; González-Flores, D.; Dau, H., Geometric distortions in nickel (oxy) hydroxide  
789 electrocatalysts by redox inactive iron ions. *Energy & Environmental Science* **2018**.
- 790 40. Li, Y.-F.; Selloni, A., Mechanism and Activity of Water Oxidation on Selected Surfaces of  
791 Pure and Fe-Doped NiOx. *ACS Catal.* **2014**, *4* (4), 1148-1153.
- 792 41. Conesa, J. C., Electronic Structure of the (Undoped and Fe-Doped) NiOOH O<sub>2</sub> Evolution  
793 Electrocatalyst. *The Journal of Physical Chemistry C* **2016**, *120* (34), 18999-19010.
- 794 42. Xiao, H.; Shin, H.; Goddard, W. A., Synergy between Fe and Ni in the optimal performance  
795 of (Ni,Fe)OOH catalysts for the oxygen evolution reaction. *Proceedings of the National*  
796 *Academy of Sciences* **2018**, *115* (23), 5872-5877.
- 797 43. Kuai, L.; Geng, J.; Chen, C.; Kan, E.; Liu, Y.; Wang, Q.; Geng, B., A Reliable Aerosol-  
798 Spray-Assisted Approach to Produce and Optimize Amorphous Metal Oxide Catalysts for  
799 Electrochemical Water Splitting. *Angewandte Chemie International Edition* **2014**, *53* (29),  
800 7547-7551.
- 801 44. Song, F.; Hu, X., Exfoliation of layered double hydroxides for enhanced oxygen evolution  
802 catalysis. *Nat Commun* **2014**, *5*.

- 803 45. Deng, J.; Nellist, M. R.; Stevens, M. B.; Dette, C.; Wang, Y.; Boettcher, S. W., Morphology  
804 Dynamics of Single-Layered Ni(OH)<sub>2</sub>/NiOOH Nanosheets and Subsequent Fe Incorporation  
805 Studied by in Situ Electrochemical Atomic Force Microscopy. *Nano Letters* **2017**.
- 806 46. Dette, C.; Hurst, M. R.; Deng, J.; Nellist, M. R.; Boettcher, S. W., Structural Evolution of  
807 Metal (Oxy)hydroxide Nanosheets during the Oxygen Evolution Reaction. *ACS Applied*  
808 *Materials & Interfaces* **2018**.
- 809 47. Huang, J.; Han, J.; Wang, R.; Zhang, Y.; Wang, X.; Zhang, X.; Zhang, Z.; Zhang, Y.; Song,  
810 B.; Jin, S., Improving Electrocatalysts for Oxygen Evolution Using Ni<sub>x</sub>Fe<sub>3-x</sub>O<sub>4</sub>/Ni Hybrid  
811 Nanostructures Formed by Solvothermal Synthesis. *ACS Energy Letters* **2018**, 3 (7), 1698-  
812 1707.
- 813 48. Candelaria, S. L.; Bedford, N. M.; Woehl, T. J.; Rentz, N. S.; Showalter, A. R.; Pylypenko,  
814 S.; Bunker, B. A.; Lee, S.; Reinhart, B.; Ren, Y.; Ertem, S. P.; Coughlin, E. B.; Sather, N. A.;  
815 Horan, J. L.; Herring, A. M.; Greenlee, L. F., Multi-Component Fe–Ni Hydroxide  
816 Nanocatalyst for Oxygen Evolution and Methanol Oxidation Reactions under Alkaline  
817 Conditions. *ACS Catal.* **2017**, 7 (1), 365-379.
- 818 49. Hall, D. S.; Lockwood, D. J.; Bock, C.; MacDougall, B. R., Nickel hydroxides and related  
819 materials: a review of their structures, synthesis and properties. *Proceedings. Mathematical,*  
820 *Physical, and Engineering Sciences / The Royal Society* **2015**, 471 (2174), 20140792.
- 821 50. Gao, M.; Sheng, W.; Zhuang, Z.; Fang, Q.; Gu, S.; Jiang, J.; Yan, Y., Efficient Water  
822 Oxidation Using Nanostructured α-Nickel-Hydroxide as an Electrocatalyst. *Journal of the*  
823 *American Chemical Society* **2014**, 136 (19), 7077-7084.
- 824 51. Sun, S.; Zeng, H.; Robinson, D. B.; Raoux, S.; Rice, P. M.; Wang, S. X.; Li, G.,  
825 Monodisperse MFe<sub>2</sub>O<sub>4</sub> (M = Fe, Co, Mn) Nanoparticles. *Journal of the American Chemical*  
826 *Society* **2004**, 126 (1), 273-279.
- 827 52. Chen, S.; Si, R.; Taylor, E.; Janzen, J.; Chen, J., Synthesis of Pd/Fe<sub>3</sub>O<sub>4</sub> Hybrid  
828 Nanocatalysts with Controllable Interface and Enhanced Catalytic Activities for CO  
829 Oxidation. *The Journal of Physical Chemistry C* **2012**, 116 (23), 12969-12976.
- 830 53. Balasubramanian, M.; Melendres, C. A.; Mini, S., X-ray absorption spectroscopy studies of  
831 the local atomic and electronic structure of iron incorporated into electrodeposited hydrous  
832 nickel oxide films. *J. Phys. Chem. B* **2000**, 104, 4300-4306.
- 833 54. Brollo, M. E. F.; López-Ruiz, R.; Muraca, D.; Figueroa, S. J. A.; Pirota, K. R.; Knobel, M.,  
834 Compact Ag@Fe<sub>3</sub>O<sub>4</sub> Core-shell Nanoparticles by Means of Single-step Thermal  
835 Decomposition Reaction. *Scientific Reports* **2014**, 4, 6839.
- 836 55. Hartl, M.; Gillis, R. C.; Daemen, L.; Olds, D. P.; Page, K.; Carlson, S.; Cheng, Y.; Hügler, T.;  
837 Iverson, E. B.; Ramirez-Cuesta, A. J.; Lee, Y.; Muhrer, G., Hydrogen adsorption on two  
838 catalysts for the ortho- to parahydrogen conversion: Cr-doped silica and ferric oxide gel.  
839 *Physical Chemistry Chemical Physics* **2016**, 18 (26), 17281-17293.
- 840 56. Chen, J. Y. C.; Miller, J. T.; Gerken, J. B.; Stahl, S. S., Inverse spinel NiFeAlO<sub>4</sub> as a highly  
841 active oxygen evolution electrocatalyst: promotion of activity by a redox-inert metal ion.  
842 *Energy & Environmental Science* **2014**, 7 (4), 1382-1386.
- 843 57. Chen, C. L.; Dong, C.-L., X-Ray Spectroscopy Studies of Iron Chalcogenides. In  
844 *Superconductors - Materials, Properties and Applications*, Gabovich, A., Ed. InTech: Rijeka,  
845 2012; p Ch. 02.
- 846 58. Regan, T. J.; Ohldag, H.; Stamm, C.; Nolting, F.; Lüning, J.; Stöhr, J.; White, R. L.,  
847 Chemical effects at metal/oxide interfaces studied by x-ray-absorption spectroscopy.  
848 *Physical Review B* **2001**, 64 (21), 214422.

- 849 59. Chen, T.; Cao, L.; Zhang, W.; Zhang, W.; Han, Y.; Zheng, Z.; Xu, F.; Kurash, I.; Qian, H.;  
850 Wang, J. o., Correlation between electronic structure and magnetic properties of Fe-doped  
851 ZnO films. *Journal of Applied Physics* **2012**, *111* (12), 123715.
- 852 60. Kim, D. H.; Lee, H. J.; Kim, G.; Koo, Y. S.; Jung, J. H.; Shin, H. J.; Kim, J. Y.; Kang, J. S.,  
853 Interface electronic structures of BaTiO<sub>3</sub>@X nanoparticles (X= g-Fe<sub>2</sub>O<sub>3</sub>, Fe<sub>3</sub>O<sub>4</sub>, a-Fe<sub>2</sub>O<sub>3</sub>, and  
854 Fe) investigated by XAS and XMCD. *Physical Review B* **2009**, *79* (3), 033402.
- 855 61. van Aken, P. A.; Liebscher, B., Quantification of ferrous/ferric ratios in minerals: new  
856 evaluation schemes of Fe L<sub>23</sub>electron energy-loss near-edge spectra. *Physics and Chemistry*  
857 *of Minerals* **2002**, *29* (3), 188-200.
- 858 62. Tan, H.; Verbeeck, J.; Abakumov, A.; Van Tendeloo, G., Oxidation state and chemical shift  
859 investigation in transition metal oxides by EELS. *Ultramicroscopy* **2012**, *116*, 24-33.
- 860 63. Chen, J.; Huang, D. J.; Tanaka, A.; Chang, C. F.; Chung, S. C.; Wu, W. B.; Chen, C. T.,  
861 Magnetic circular dichroism in Fe 2*p* resonant photoemission of magnetite. *Physical Review*  
862 *B* **2004**, *69* (8), 085107.
- 863 64. Zhao, W.; Li, M.; Chang, C.-Z.; Jiang, J.; Wu, L.; Liu, C.; Moodera, J. S.; Zhu, Y.; Chan, M.  
864 H. W., Direct imaging of electron transfer and its influence on superconducting pairing at  
865 FeSe/SrTiO<sub>3</sub> interface. *Science Advances* **2018**, *4* (3).
- 866 65. Klaus, S.; Cai, Y.; Louie, M. W.; Trotochaud, L.; Bell, A. T., Effects of Fe electrolyte  
867 impurities on Ni(OH)<sub>2</sub>/NiOOH structure and oxygen evolution activity. *J. Phys. Chem. C*  
868 **2015**, *119*, 7243-7254.
- 869 66. Bau, J. A.; Lubner, E. J.; Buriak, J. M., Oxygen Evolution Catalyzed by Nickel–Iron Oxide  
870 Nanocrystals with a Nonequilibrium Phase. *ACS Applied Materials & Interfaces* **2015**, *7* (35),  
871 19755-19763.
- 872 67. Smith, R. D. L.; Berlinguette, C. P., Accounting for the Dynamic Oxidative Behavior of  
873 Nickel Anodes. *Journal of the American Chemical Society* **2016**, *138* (5), 1561-1567.
- 874 68. Trotochaud, L.; Young, S. L.; Ranney, J. K.; Boettcher, S. W., Nickel–Iron Oxyhydroxide  
875 Oxygen-Evolution Electrocatalysts: The Role of Intentional and Incidental Iron Incorporation.  
876 *Journal of the American Chemical Society* **2014**, *136* (18), 6744-6753.

877



The 3-D morphology plays a key role in optimization of the electrocatalytic activity and stability of the nanocatalyst for OER.

